



Applied Computational
Electromagnetics Society



Newsletter
Volume 19 – No. 3
ISSN 1056-9170



November 2004



APPLIED COMPUTATIONAL ELECTROMAGNETICS SOCIETY (ACES)

NEWSLETTER

Vol. 19 No. 3

November 2004

TABLE OF CONTENTS

THE PRATICAL CEMist “Computer Tool for ATU Loss Estimation” W. Perry Wheless	6
TECHNICAL FEATURE ARTICLE “Computational Aspects in Analyzing the Efficient Utilization of the RF Transmission Hyperspace” Andrew L. Drozd, Chilukuri K. Nohan, Pramod K. Varshney, Donald D. Weiner.....	10
TUTORIAL ARTICLE “A Review of the Path Integral Time Domain Method Jeffrey A. Miller	19
APPLICATION ARTICLE “Coplanar Waveguide Fed Bow-Tie Slot Antennas for Wideband Operations” Abdelnasser A. Eldek, Atef Z. Elsherbeni, Charles E. Smith	45
Call for Papers 2005 IEEE/ACES International Conference	52
ANNOUNCEMENTS:	
ADVERTISING Rates.....	53
DEADLINE to Submission of Articles	53
Last Word	53

PERMANENT STANDING COMMITTEES OF ACES, INC.

COMMITTEE	CHAIRMAN	ADDRESS
NOMINATION	Rene Allard	Penn State University PO Box 30 State College, PA 16804-0030 rja5@psu.edu
ELECTIONS	Rene Allard	Penn State University PO Box 30 State College, PA 16804-0030 rja5@psu.ed
FINANCE	Andrew Peterson	Georgia Institute of Technology School of ECE Atlanta, GA 30332-0250 peterson@ece.gatech.edu
PUBLICATIONS	Atef Elsherbeni	EE Department, Anderson Hall University of Mississippi University, MS 38677 atef@olemiss.edu
CONFERENCE	Osama Mohammed	Florida International University ECE Department Miami, FL 33174 mohammed@fiu.edu
AWARDS	Ray Perez	Martin Marietta Astronautics MS 58700, PO Box 179 Denver, CO 80201 ray.j.perez@lmco.com

MEMBERSHIP ACTIVITY COMMITTEES OF ACES, INC. INC.
--

COMMITTEE	ADDRESS	CHAIRMAN
SOFTWARE VALIDATION	Bruce Archambeault	IBM 3039 Cornwallis Road, PO Box 12195 Dept. 18DA B306 Research Triangle Park, NC 27709
HISTORICAL	Robert Bevensee	BOMA Enterprises PO Box 812 Alamo, CA 94507-0812 rmbevensee@cs.com
CONSTITUTION and BYLAWS	Leo Kempel	2120 Engineering Building Michigan State University East Lansing, MI 48824 kempel@egr.msu.edu
MEMBERSHIP and COMMUNICATIONS	Vicente Rodriguez	ETS-LINDGREN L.P. 1301 Arrow Point Drive Cedar Park, TX 78613 rodriguez@ieee.org
INDUSTRY RELATIONS	Andy Drozd	ANDRO Consulting Services PO Box 543 Rome, NY 13442-0543 Andro1@aol.com

ACES NEWSLETTER STAFF

EDITOR-IN-CHIEF, NEWSLETTER

Bruce Archambeault
IBM
3039 Cornwallis Road, PO Box 12195
Dept. 18DA B306
Research Triangle Park, NC 27709
Phone: 919-486-0120
email: barch@us.ibm.com

EDITOR-IN-CHIEF, PUBLICATIONS

Atef Elsherbeni
EE Department, Anderson Hall
University of Mississippi
University, MS 38677
Email: atef@olemiss.edu

ASSOCIATE EDITOR-IN-CHIEF

Ray Perez
Martin Marietta Astronautics
MS 58700, PO Box 179
Denver, CO 80201
Phone: 303-977-5845
Fax: 303-971-4306
email: ray.j.perez@lmco.com

MANAGING EDITOR

Richard W. Adler
Naval Postgraduate School/ECE Dept.
Code ECAB, 833 Dyer Road,
Monterey, CA 93943-5121
Phone: 831-646-1111
Fax: 831-649-0300
email: rwa@attglobal.net

EDITORS

CEM NEWS FROM EUROPE

Tony Brown
University of Manchester
PO Box 88 Sackville Street
Manchester M60 1QD United Kingdom
Phone: +44 (0) 161-200-4779
Fax: +44 (0) 161-200-8712
email: Anthony.brown@manchester.ac.uk

TECHNICAL FEATURE ARTICLE

Andy Drozd
ANDRO Consulting Services
PO Box 543
Rome, NY 13442-0543
Phone: 315-337-4396
Fax: 314-337-4396
email: androl@aol.com

THE PRACTICAL CEMIST

W. Perry Wheless, Jr.
University of Alabama
PO Box 11134
Tuscaloosa, AL 35486-3008
Phone: 205-348-1757
Fax: 205-348-6959
Email: wwheless@ualvm.ua.edu

MODELER'S NOTES

Gerald Burke
Lawrence Livermore National Labs.
Box 5504/L-156
Livermore, CA 94550
Phone: 510-422-8414
Fax: 510-422-3013
email: burke2@llnl.gov

PERSPECTIVES IN CEM

Manos M. Tentzeris
Georgia Institute of Technology
ECE Dept.
Atlanta, GA 30332-0250
Phone: 404-385-0378
email: centze@ece.gatech.edu

TUTORIAL

J. Alan Roden
IBM Microelectronics
Dept. OSXA
3039 Cornwallis Road
Research Triangle Park, NC 27709
Phone: 919-543-8645
email: jaroden@us.ibm.com

ACES JOURNAL

EDITOR IN CHIEF

Atef Elsherbeni
Associate Editor-in-Chief Journal, Alexander Yakovlev
EE Department, Anderson Hall
University of Mississippi
University, MS 38677
Phone: 662-915-5382
email: atef@olemiss.edu

NEWSLETTER ARTICLES AND VOLUNTEERS WELCOME

The ACES Newsletter is always looking for articles, letters and short communications of interest to ACES members. All individuals are encouraged to write, suggest or solicit articles either on a one-time or continuing basis. Please contact a Newsletter Editor.

AUTHORSHIP AND BERNE COPYRIGHT CONVENTION

The opinions, statements and facts contained in this Newsletter are solely the opinions of the authors and/or sources identified with each article. Articles with no author can be attributed to the editors or to the committee head in the case of committee reports. The United States recently became part of the Berne Copyright Convention. Under the Berne Convention, the copyright for an article in this newsletter is legally held by the author(s) of the article since no explicit copyright notice appears in the newsletter.

BOARD OF DIRECTORS

EXECUTIVE COMMITTEE

Osama Mohammed, President	Allen W. Glisson, Treasurer
Tapan Sakar, Vice President	Richard W. Adler, Executive Officer
Keith Lysiak, Secretary	

DIRECTORS-AT-LARGE

Allen W. Glisson	2005	Leo Kemple	2006	Randy Haupt	2007
Keith Lysiak	2005	Osama Mohammed	2006	Juan Mosig	2007
Eric Mechielssen	2005	Tapan Sarkar	2006	Omar Ramahi	2007

ACES ELECTRONIC PUBLISHING GROUP

Atef Elsherbeni	Electronic Publishing Managing Editor
Matthew J. Inman	Site Administrator
Orin H. Council	Contributing Staff
Imran Kader	Past Site Administrator
Brad Baker	Past Staff
Jessica Drewrey	Past Staff
Chris Riley	Past Staff

Visit us on line at:
<http://aces.ee.olemiss.edu>

Computer Tool for ATU Loss Estimation

W. Perry Wheless, Jr.
 Department of Electrical and
 Computer Engineering
 University of Alabama
 Tuscaloosa, AL 35487
 Email: wwheless@coe.eng.ua.edu

Abstract—Antenna tuning units (ATUs) using Tee networks are in widespread use by practical radio communicators throughout the HF (3-30 MHz) and VHF (30-300 MHz) spectrum. A computer software tool for estimating the power losses in such networks in general impedance matching applications has been developed. The program is described here, and illustrative case study results are reported.

I. INTRODUCTION

The Tee-network ATU, shown in Fig. 1 with antenna feedpoint load $Z_{in} = R_A + jX_A$, is a classic approach to antenna impedance matching in practical HF and VHF radio applications. For discussion here, the coaxial line from the transmitter is assumed to be of characteristic impedance $Z_0 = Z_{line} = 50\Omega$. Further, it is assumed that all network voltages and currents are specified with RMS values.

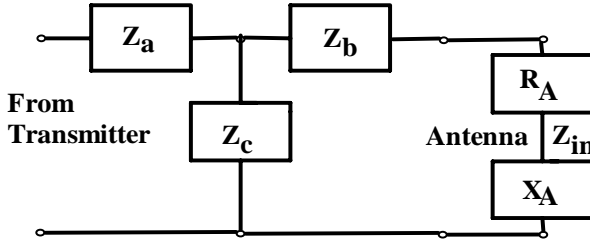


Figure 1. Tee-network Antenna Tuning Unit.

If the load (that is, antenna feed point) is purely resistive with value R_A , a $\frac{\lambda}{4}$ transmission line section of characteristic impedance $Z_{xfmr} = \sqrt{Z_0 \cdot R_A}$ will produce the desired impedance match at the design frequency. The Tee network components, idealized for the lossless case, are then pure reactances

$$|Z_a| = |Z_b| = |Z_c| = \sqrt{Z_0 \cdot R_A} \quad (1)$$

[1] with Z_c of opposite sign from Z_a and Z_b ; this results in a lumped element circuit equivalent to a $\frac{\lambda}{4}$ section of transmission line of appropriate characteristic impedance. Interested readers can find more complete background in [2], where it is shown that the impedance matrix for a section of lossy transmission line with propagation constant $\gamma = \alpha + j\beta$ and

length d is

$$Z = \begin{bmatrix} Z_a + Z_c & Z_c \\ Z_c & Z_b + Z_c \end{bmatrix} = \begin{bmatrix} Z_0 \coth \gamma d & \frac{Z_0}{\sinh \gamma d} \\ \frac{Z_0}{\sinh \gamma d} & Z_0 \coth \gamma d \end{bmatrix} \quad (2)$$

Simplifying to the lossless case,

$$Z_a = Z_b = jZ_0 \tan \beta \frac{d}{2}; \quad Z_c = -jZ_0 \csc \beta d. \quad (3)$$

With $\beta = \frac{2\pi}{\lambda}$ and $d = \frac{\lambda}{4}$, the results in [1] follow directly.

Fig. 2 shows more Tee-network ATU circuit detail, for the case of inductive input and output legs and a capacitive shunt leg reactance. It is also possible to have the input/output legs capacitive with the shunt leg inductive as an alternative, but the Fig. 2 configuration is preferred for use with radio transmitters because its low-pass filter behavior attenuates the harmonic output produced (to varying degrees) by all high-power rf amplifiers.

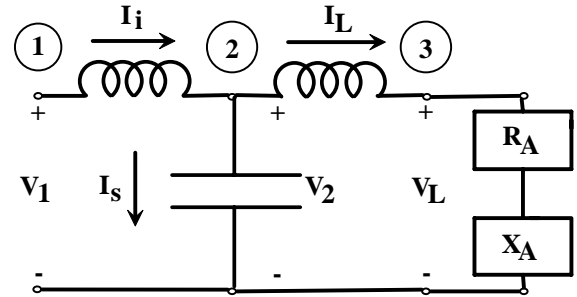


Figure 2. More detailed ATU circuit.

For the moment, the premise is continued that $X_A = 0$, so antenna $Z_{in} = R_A$ is purely resistive. Analysis of the Fig. 2 network with conventional circuit theory to obtain voltage and current expressions is then straightforward. However, the results are of limited utility because, at this point, the reactances are lossless and the load purely real.

II. EXTENSION TO COMPLEX LOAD

Generally, $X_A \neq 0$ and antenna feed $Z_{in} = R_A + jX_A$. In this case, the standard practice is to use the driving-point reactance jX_A to make up part of $Z_b = jX_2$ from Fig. 1, with total value X_2 calculated according to Eqn. 1. Hence, the reactance actually placed in output leg “b” of the ATU is

$$X'_2 = X_2 - X_A. \quad (4)$$

III. EXTENSION TO LOSSY REACTANCES

With the above procedure of routinely incorporating X_A into the ATU's output leg reactance $Z_b = jX_2$, the impedance matching task is reduced to matching a real load to a real transmission line characteristic impedance Z_0 , which has been specified to be 50Ω throughout this discussion. Denoting inductance Q-factor by Q_L and capacitor Q-factor by Q_C according to the most fundamental specification of Q

$$Q = \frac{\text{reactance in Ohms}}{\text{resistance in Ohms}} \quad (5)$$

allows the calculation of lossy reactive element resistances through

$$R_L = R_{ind} = \frac{jX_L}{Q_L} \text{ and } R_C = R_{cap} = \left| \frac{-jX_C}{Q_C} \right|. \quad (6)$$

In Fig. 3 below, a dashed line appears through the block previously occupied by X_A to represent replacement by a short-circuit connection, jX_2 in the ATU output leg has been changed to jX'_2 to indicate incorporation of X_A into X_2 , and the three lossy reactance resistances are denoted by R_1 , R_2 , and R_3 .

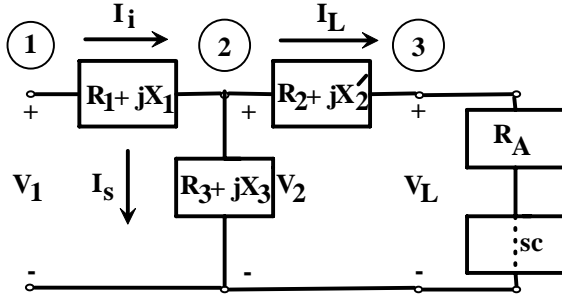


Figure 3. Lossy ATU.

The introduction of component losses requires a more robust solution strategy, as the application conditions for Eqn. 1 are now violated, and its guidance is now potentially highly unreliable and inaccurate. An analytical attempt at solution of the new, real-world problem quickly becomes egregiously heinous, and a computer-based numerical solution is highly preferable.

IV. PROGRAM EQUATIONS AND STRATEGY

Even in the lossy element case, it remains practical to readily obtain 1:1 SWR at the connection of the transmitter output coax to the ATU input for the vast majority of, if not for all, complex antenna Z_{in} impedances. However, as practical radio communicators know, obtaining a matched-impedance condition now generally is an experimental adjustment procedure under human operator or microprocessor control, monitoring input SWR value as ATU reactance values are varied.

The computer program objectives are (1) given Q_L and Q_C , determine reactance values $X_1 - X_3$ that will give a matched impedance condition between antenna and coaxial rf feed, and (2) determine the percent power dissipated in each of the

three ATU legs, as well as in the antenna feed resistance R_A . Note that R_A is actually a series combination of ohmic loss and radiation resistance, and separation of the two is beyond the scope of this study. The reader should note that, for this particular study, all ATU inductors are assumed to have the same Q_L , and all capacitors are assumed to have the same Q_C .

Since an accounting for the percent distribution of rf input power is sought, the numerical value of input power P_{in} is immaterial, and is set to 100 Watts in the code. Relations for the network voltages and currents are developed below.

Refer to Fig. 3, recalling Eqn. 4 said $X_2 = X'_2 + X_A$ and keeping in mind that X_A physically is in the antenna feedpoint load. Assume (i) a matched condition to $Z_0 = 50$ is achieved, (ii) input power P_{in} is specified, (iii) RMS values of voltage and current are used, and (iv) the ATU shunt leg is capacitive while the input and output legs are inductive. By Ohm's Law,

$$P_{in} = I_i^2 Z_0 = \frac{V_1^2}{Z_0} \Rightarrow I_i = \sqrt{\frac{P_{in}}{Z_0}} \text{ and } V_1 = \sqrt{P_{in} \cdot Z_0}. \quad (7)$$

Then, by current division,

$$I_S = I_i \frac{(R_2 + R_A + jX_2)}{(R_2 + R_A + jX_2) + (R_3 - jX_3)} \quad (8)$$

and

$$V_2 = (I_S) (R_3 - jX_3). \quad (9)$$

Applying current division again, this time to the output leg feeding the antenna:

$$I_L = I_i \frac{(R_3 - jX_3)}{(R_2 + R_A + jX_2) + (R_3 - jX_3)} \quad (10)$$

and

$$V_L = I_L (R_A + jX_A). \quad (11)$$

Computed $Z_{in calc}$ at the ATU input is from

$$Z_{in calc} = (R_1 + jX_1) + \frac{(R_2 + R_A + jX_2)(R_3 - jX_3)}{(R_2 + R_A + jX_2) + (R_3 - jX_3)} \quad (12)$$

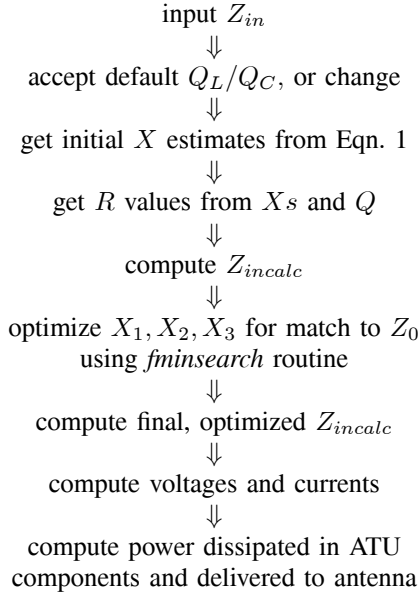
Because the component resistances are now coupled into the equations and those resistances, in turn, depend on the corresponding component reactances, the cause for analytical difficulty and need for numerical aid is apparent.

As noted earlier, Eqn. 1 is inaccurate and unreliable in the lossy case with significant antenna mismatch, but it does provide a useful initial estimate for the three ATU reactances. MATLAB [3] includes an optimization function *fminsearch.m* in its Optimization Toolbox library which can be employed to find the minimum of an unconstrained multivariable function $\min_x f(x)$, where x is a vector and $f(x)$ is a function that returns a scalar. The "multivariable" values to be optimized are those for X_1 , X_2 , and X_3 , and the returned scalar is the absolute value of the difference between the desired 50Ω input and the calculated ATU input impedance at each iteration of the reactance values. For each iteration,

$$R_1 = \left| \frac{X_1}{Q_L} \right| \text{ or } R_1 = \left| \frac{X_1}{Q_C} \right|, \quad (13)$$

depending on whether X_1 is inductive/positive or capacitive/negative for that particular iteration. Similar arithmetic is also applied for R_3 and R_2 , noting that X'_2 and not X_2 is the numerator for calculating R_2 because the primed value is that actually placed in the ATU output leg. Note also that although we are starting with a network with positive input and output leg reactances and a negative shunt leg reactance, the matching optimization routine may occasionally change the sign of one or more of the components.

Default values of Q_L and Q_C are set in the computer tool to 100 and 1000, respectively, but the user is prompted and offered the opportunity to change either value when the program is executed. The code essentially implements the following sequence:



Optimized ATU input impedances are not generally *exactly* $50 + j0\Omega$, but are so close that reflected power from the ATU input port is insignificant.

V. ILLUSTRATIVE RESULTS

Case 1: Antenna $Z_{in} = 72 + j43\Omega$, typical of a $\frac{\lambda}{2}$ dipole. Using default Q s, program execution yields the following results:

Case 1: $Q_L = 100, Q_C = 1000$	
Initial $X_1 - X_3$	+60, +60, -60 Ω
Optimized $X_1 - X_3$	+60.507, +61.023, -59.708 Ω
Initial Z_{incalc}	50.501 + j0.099682 Ω
Optimized Z_{incalc}	50.000 + j3.6275e-6 Ω
Final $R_1 - R_3$	0.60507, 0.18023, 0.059708 Ω
ATU input leg power	1.2101 %
ATU shunt leg power	0.20436 %
ATU output leg power	0.24617%
Power delivered to antenna	98.33937 %
Total power	100.000%
Total ATU loss	0.073 dB

For the remaining case studies, power percents are rounded to the nearest tenth.

Case 2: Antenna $Z_{in} = 20 - j300\Omega$, a moderately mismatched small antenna.

Case 2: $Q_L = 100, Q_C = 1000$	
Initial $X_1 - X_3$	+31.62, +31.62, -31.62 Ω
Optimized $X_1 - X_3$	+29.986, +32.254, -34.177 Ω
Initial Z_{incalc}	43.2 + j0.086 Ω
Optimized Z_{incalc}	50.0 - j3.93e-7 Ω
Final $R_1 - R_3$	0.299, 3.323, 0.034 Ω
ATU input leg power	0.6 %
ATU shunt leg power	0.2 %
ATU output leg power	14.1 %
Power delivered to antenna	85.1 %
Total power	100.000%
Total ATU loss	0.70 dB

Case 3: Antenna $Z_{in} = 11.7 + j0\Omega$, a self-resonant normal mode helical antenna (NMHA) of length 0.05λ , as described on page 68 of reference [4].

Case 3: $Q_L = 100, Q_C = 1000$	
Initial $X_1 - X_3$	+24.19, +24.19, -24.19 Ω
Optimized $X_1 - X_3$	+24.07, +24.34, -24.4 Ω
Initial Z_{incalc}	49.15 + j 0.098 Ω
Optimized Z_{incalc}	50.00 + j4.75e-6 Ω
Final $R_1 - R_3$	0.241, 0.243, 0.024 Ω
ATU input leg power	0.5 %
ATU shunt leg power	0.3 %
ATU output leg power	2.0 %
Power delivered to antenna	97.2 %
Total power	100.000%
Total ATU loss	0.12 dB

Case 4: Antenna $Z_{in} = 0.49 - j900\Omega$ for a short dipole reported by [5] and further considered in [4].

Case 4: $Q_L = 100, Q_C = 1000$	
Initial $X_1 - X_3$	+49.5, +49.5, -49.5 Ω
Optimized $X_1 - X_3$	+0.12, +19.8, -24.5 Ω
Initial Z_{incalc}	2.62 + j5.13e-3 Ω
Optimized Z_{incalc}	50.0 + j1.18e-5 Ω
Final $R_1 - R_3$	0.0012, 9.198, 0.0245 Ω
ATU input leg power	0.0 %
ATU shunt leg power	0.3 %
ATU output leg power	94.7 %
Power delivered to antenna	5.0 %
Total power	100.000%
Total ATU loss	12.97 dB

The computer tool result of 5.0% power delivered to the antenna agrees with the tabulated value on p. 68 of [4]. NOTE: Case 4 was also run with $Q_L = 400$ for comparison with [4]. The full table of results is omitted in the interest of brevity, but the total power (efficiency) came out 18%, again in agreement with Fujimoto, and the total ATU loss was 7.54 dB.

Case 5: Antenna $Z_{in} = 0.001 + j11000\Omega$. This is an extreme case of a 1 mH inductor being driven at 1.8 MHz through an ATU. The resistance value is synthetic, for illustration purposes only, and the radiation resistance is likely even smaller. Turns of the coil are necessarily tightly wound, resulting in high proximity effect losses, and the coupling of the coil to ground will also cause a loss resistance to appear in series at the feed terminals. An actual inductor approximating this case has been constructed, requiring approximately 285 turns of insulated #14 electrical wire in a single layer, with adjacent turns touching, on a nominal 4-inch diameter PVC pipe core. The measured inductance was 1.2 mH. In a rudimentary experiment, the inductive load did radiate, at a level 50-60 dB down from a dipole but sufficient to establish an interstate radio link under favorable noise and interference conditions.

The cited coil terminal resistance of 0.001 Ohm is not a value realistically expected to be observed but, at the same time, is optimistic for a radiation resistance value in this case.

Case 5: $Q_L = 100, Q_C = 1000$	
Initial $X_1 - X_3$	+0.224, +0.224, -0.224 Ω
Optimized $X_1 - X_3$	+64.6, +36.8, -28.8 Ω
Initial $Z_{in\text{calc}}$	0.007 + j9.1e-6 Ω
Optimized $Z_{in\text{calc}}$	50.0 + j2.45e-5 Ω
Final $R_1 - R_3$	0.65, 10.96, 0.03 Ω
ATU input leg power	1.3 %
ATU shunt leg power	0.5 %
ATU output leg power	98.2 %
Power delivered to antenna	9e-3 %
Total power	100.000%
Total ATU loss	40.5 dB

As expected, the ATU loss is enormous. For a real load device similar to that described, again, the observed input resistance would be much higher and the resulting ATU loss in dB much lower. However, this would be deceptive as nearly all the power delivered to the antenna terminals in that instance would be actually dissipated in ohmic loss versus radiation.

VI. PROGRAM AVAILABILITY

Copies of the MATLAB code are available from the author on request by email. Please enter "ATU MATLAB code" in the email subject line. Further, please be advised that prospective users must have not only base MATLAB, but also the Optimization Toolbox, available to them.

VII. CONCLUDING REMARKS

Given accurate Q_L and Q_C values, the computer tool for ATU loss estimation described here has produced useful results in numerous test applications. Clearly, however, the reliability of the output depends directly on the precision of Q specifications. It has proved challenging to discern better "typical" Q_L and Q_C values for real components operating in the HF-VHF spectrum than those entered as the default numbers in the present code. Equipment is relatively available for measuring Q values and, because they are so important, ATU designers

and users are urged to expend the time and effort necessary to obtain measured data. Individuals willing to share their experiences, data, and/or conclusions about appropriate default inductor and capacitor Q values are encouraged to contact the author.

REFERENCES

- [1] Layton, Jack, *Directional Broadcast Antennas: A Guide to Adjustment, Measurement, and Testing*, TAB Books, Blue Ridge Summit, PA, 1974, p. 123.
- [2] Brown, R.G., Sharpe, R.A., Hughes, W.L., and Post, R.E., *Lines, Waves, and Antennas - The Transmission of Electric Energy, 2nd Edition*, John Wiley & Sons, New York, 1973, pp. 160 and 112.
- [3] MATLAB is a registered trademark of The Mathworks, Natick, MA.
- [4] Fujimoto, K., Henderson, A., Hirasawa, K., and James, J.R., *Small Antennas*, John Wiley & Sons, New York, 1987, p. 68.
- [5] King, R.W.P., *The Theory of Linear Antennas*, Harvard University Press, Cambridge, MA, 1950.

COMPUTATIONAL ASPECTS IN ANALYZING THE EFFICIENT UTILIZATION OF THE RF *TRANSMISSION HYPERSPACE*

Andrew L. Drozd[†], Chilukuri K. Mohan^{*}, Pramod K. Varshney^{*} and Donald D. Weiner^{*}

Abstract

New approaches for enhancing spectrum utilization and frequency management for large, complex systems have recently been investigated. These approaches enable the effective and efficient joint utilization of all orthogonal electromagnetic (EM) transmission resources, including, but not limited to time, frequency, geographic space, modulation/code, and polarization. This multi-dimensional environment is hereafter referred to as the *Transmission Hyperspace (TH)*, a term intended to convey the notion of a multi-dimensional resource space (with n degrees of freedom expressed as an n -tuple) in which each dimension allows orthogonality amongst users. The challenges to the modeling and solution of large-scale *TH*-based problems are presented in the context of assigning the n -tuple dimensions in near real time. Also described are the key aspects of the multi-dimensional *Transmission Hyperspace* and approaches for efficient spectrum management, the results of which are expected to garner several orders of magnitude improvement in RF resource utilization and therefore, aggregate information throughput.

INTRODUCTION

EM propagation at RF frequencies is currently governed by a one-dimensional “real estate” approach to the allocation of frequency bands, where the licensee has specific legal right to transmit within a band. The entire spectrum from 3 kHz to 30 GHz is currently allocated in this fashion. Unfortunately, this “set-it-and-forget-it” management scheme is straining under the immense pressure of exponentially increasing demand by burgeoning numbers of various types of wireless devices, spanning commercial and military applications all the way from short range home networks and cordless phones to the global communications grid. Given the finite nature of the

RF frequency spectrum, it is desired that alternative approaches to the management of the resource be explored.

One approach involves exploiting optimization and orthogonality schemes that allow for multiple users to operate without interference. These schemes leverage several techniques in unison such as time slicing, frequency division multiplexing, use of smart directional antennas, application of new spread spectrum codes, and polarization diversity. Conceivable approaches to a system for joint optimization of the multiple orthogonalizing transmission parameters show that no two (or more) users are transmitting at the same time, even though they may be using the same frequency in the same space with the same spread spectrum code. Similar illustrations include the case of a spatially orthogonalized system in terms of transmit beam patterns that do not overlap and cross-polarized waves in ideal cases.

The *Transmission Hyperspace (TH)* concept takes advantage of optimization and orthogonality schemes to permit multiple users to operate without interference. The concept applies operations research theory and multiobjective joint optimization algorithms assisted by knowledge base technologies, novel frequency- and time-domain interference rejection models, and waveform diversity techniques to analyze dimensional “synergy” and “prioritize” the *TH* cell dimensions. This includes the limited application of joint time-frequency transforms.

One of the challenges being faced in the design and implementation of this concept is that of ensuring computational efficiency. The *TH* paradigm includes an electromagnetic interference monitor/analyzer that effectively determines the RF links and signal strengths in the presence of ambient interference, and then computes the various environmental interactions to assist in assigning and managing the RF resource space.

[†] ANDRO Computational Solutions, LLC, Beeches Technical Campus, Rome, NY USA, adrozd@androcs.com.

^{*} Syracuse University, EECS Dept. Syracuse, NY USA, mohan@ecs.syr.edu, varshney@ecs.syr.edu, ddweiner@ecs.syr.edu.

THE TRANSMISSION HYPERSPACE

The *TH* concept can be imagined as an electromagnetically occupied volume bounded in all dimensions (time, space, frequency, code/modulation, polarization, etc.), or a “cube” (in more than three dimensions), as shown in Figure 1. Here, the cube is constantly changing with “cells” of signals that have applied for, received, used, and returned their transmission coordinates. When one wants to transmit, one asks for the coordinates, then transmits and goes off the air. Someone else then fills in or occupies that cell and the new or current user gets another cell the next time through the cycle. Using this approach, it can be shown that unused spectrum changes in *time* and *space*.

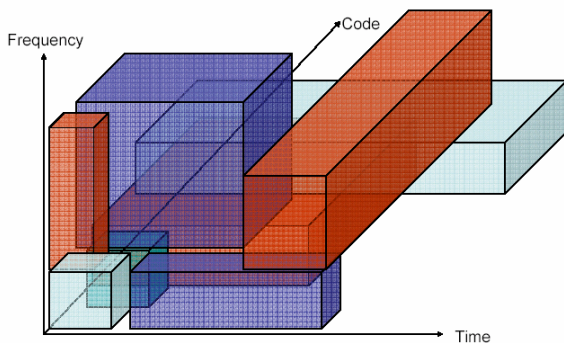


Figure 1: Geometric Representation of the *TH* Concept (Constrained to 3-D).

Currently, there are no known technological approaches to RF transmission in spectrum management that consider all of these dimensions jointly, and certainly none that consider them in the context of a system optimization problem.

Furthermore, these approaches have taken into account existing spectrum policies and ideas being pursued in government, academia, and industry, the subset of which includes the obvious solutions such as: a single centralized global broker of *TH* cells, multiple distributed and coordinated local brokers of *TH* cells for local users, ad-hoc “mesh” networking, fixed assignment, and hybrid approaches.

Multiobjective Optimization Approaches

There are a number of possible approaches to achieving multiobjective joint optimization. Statistical optimization is one approach. Linear

and nonlinear optimization, meta-heuristics, constraint satisfaction, and multidisciplinary optimization are yet others. Potential solutions to the multiobjective joint optimization problem are founded in the industrial engineering, operations research, and geoscience disciplines.

An important distinction between *multiobjective* and *joint* optimization should be made before proceeding here. First, multiobjective joint optimization refers to a procedure for determining the “best fit” of decision variables that satisfy a given cost or objective function in an optimal way. In general, the basis of this approach is the application of mathematical algorithms founded in operations research theory; in this case, to arrive at techniques for improving spectrum efficiency utilizing flexible and adaptive communications technologies—the overall objective. For example, one can optimally assign the multiple dimensions of an electromagnetic signal or waveform in a *joint* manner to ensure that multiple objectives are met, such as maximizing RF point-to-point connectivity and availability, improving signal-to-interference-plus-noise ratio (SINR) or the interference rejection capacity of systems, and optimizing the mobility of systems in the overall spectrum management scheme while reducing power consumption, latency, and operational cost. Other potential approaches include methods to extend the frequency agility of software defined radios to provide a wider set of capabilities for dynamic spectrum management as a function of the RF resource space assignments.

Hence, given a set of dimensions, what can be expected as the dimensions are iteratively varied to arrive at an optimal assignment? Furthermore, how does changing one dimension affect all other dimensions? The application of joint optimization schemes will help answer these questions. Also, given the placement of one or more transmitters in a “spectral environment,” how can radio channel assignments and efficient solutions of network design problems be optimized? The knowledge to be gained here will lead to the identification of ways to optimize the RF communications process for real world situations.

Let us further consider the multiobjective problem. Research in the domain of data analysis and knowledge discovery in multivariate databases has demonstrated the applicability of information systems for geophysical databases to support

collaborative research tasks—which exemplifies a type of multiobjective problem. Novel indexing and abstraction techniques have been studied for efficient search and monitoring of massive data sets. This includes the optimization of complex spatial-temporal queries and rules using knowledge-based data mining (i.e., intelligent searching for patterns in data, cataloguing and retrieval of information, data management, and query optimization). Implementations based on mass-storage systems and an intelligent front-end have been investigated using Supercomputer testbeds for parallel search and computationally-intensive functions.

Why be concerned with ensuring computational efficiency in this case? The answer lies in our desire to implement new technologies that can automatically *sense, analyze, interpret, and decide* (SAID) about the nature of the EM environment in real time both efficiently and accurately—a challenging goal indeed! This is key to effectively designing a real time environmental monitoring and analysis system that can collect a wealth of environmental data and performs subsequent decision making on the multi-dimensional data to arrive at a *best-fit* solution to a given RF communications or multi-spectral sensors problem.

The present problem is one of optimization that requires assigning user requests to regions in the RF resource space as the requests are applied for and processed. Clearly, latency or long delays in processing requests and/or responding must be minimized in this case; otherwise, the purpose of having a high-throughput, rapid-response communications system would be defeated. So the main question is: *how do we achieve computational efficiency “on the fly” for the present problem?*

It is noted that the “spectrum management” of many of today’s RF communications systems and information networks mainly involves the management of a smaller subset of the resource space dimensions; namely, time, frequency, and code and to some extent, geo-position. Typically, this invokes such techniques as Frequency-Division Multiple Access (FDMA), Time-Division Multiple Access (TDMA), and Code-Division Multiple Access (CDMA) including the use of Global Positioning System (GPS) coordinates.

The *TH* approach extends the current methods for achieving the goals of spectrum management by applying multiobjective joint optimization to the broader set of multiple dimensions of the RF resource space. One can view the application of optimization schemes for the present problem in terms of sets of intersecting parallel lines that are nearly orthogonalized with respect to each other as Figure 2 roughly illustrates.

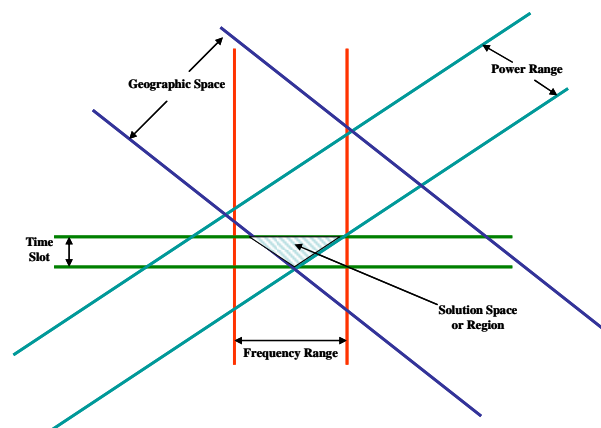


Figure 2: Generalization of the Approach for Arriving at an Optimized Solution for the Multi-Dimensional RF Resource Space.

The “assignment” of the parallel lines is somewhat arbitrary in this illustration. True or perfect mutual orthogonalization among the dimensions is not necessarily implied or enforced here for practical purposes. Each set of parallel lines represents a range for a given RF resource space dimension e.g., frequency range, time span, geographic space or region (say, for mobile transceivers), range of code/modulation diversity, and so on.

The shaded region formed by the intersection of the lines in Figure 2 represents the joint optimum solution to the multi-dimensional RF resource space problem. Of course, this is an oversimplification of the approach in that the actual process of achieving the desired result is much more involved and can be quite computationally rigorous depending on the approach (i.e., the mathematical algorithms and computational methods) utilized. Another concern is the potential computational expense involved in iterating over the problem space as well as computing the EM figures of merit that will be used as part of the forward reasoning and downstream decision making process in arriving at interference-free operational states over all time

slots, that is, to the extent practical. These additional aspects are further addressed later.

In any case, the optimization task bears a close resemblance to the NP-complete bin-packing problem [1], and can hence be explored with algorithmic approaches that have been used successfully for similar assignment problems. These include: iterative improvement techniques, simulated annealing [2], Tabu Search [3], and evolutionary algorithms [4-8].

These algorithms and approaches have largely been applied to the task of optimizing a single function, although multiobjective evolutionary algorithms have also been explored in recent years. In addition, other approaches have been suggested for multiobjective optimization, attempting to explore Pareto-optimal solutions. These include the use of weighted sum techniques, multilevel programming, homotopy techniques, goal programming, and normal-boundary intersection (NBI) [9, 10].

Unfortunately, algorithms such as NBI have very high computational requirements, making their use in real time response-critical situations impractical. Also, most existing multiobjective optimization algorithms follow a “de novo” approach whenever problem data change even a little. Nonetheless, efficient multiobjective optimization algorithms that rely on an incremental approach, reusing or modifying previously discovered solutions when small changes occur in the problem data offer a potentially useful solution. Research needs to be performed to make such algorithms more computationally efficient.

However, our purpose here is not to delve into the subtle details of these various algorithmic approaches, nor to cover the advantages and limitations of each approach. Suffice it to say that the optimization schemes mentioned above, as well as other approaches, are being studied to arrive at robust and computationally efficient ways of determining optimal solutions for various classes of *physical layer* to *network layer* RF communications and multisensor problems.

Instead, we shift our focus here on the use of efficient computer modeling and simulation techniques to analyze the “spectrum management” problem for a large number of *TH*-enable radiators, assuming some degree of

optimization has already been achieved. This approach allows us to incrementally determine the efficacy (and efficiency) of the RF resource space approach involving many devices and starting with a reasonable subset of dimensions. The original goal was to develop a proven, computationally-efficient approach for determining how the RF links can be optimally formed in the presence of electromagnetic interference, to provide a basis for implementing a real time environmental monitor/analyzer component in the *TH* design.

Described below are several of the methods that currently exploit two or more dimensions of the RF resource space. The exploitation of the multi-dimensional characteristics of the RF resource space will be discussed in terms of a computer modeling and simulation approach applied to a representative communications grid problem involving multiple RF radio and antenna systems. The goal, of course, is to use several dimensions simultaneously and to maximize overall data throughput. This discussion is prefaced by a brief review of relevant topics pertaining to electromagnetic interference/compatibility (EMI/C) and spread spectrum systems.

Mutual Orthogonality and EMC

The successful implementation of the multiobjective joint optimization implies EMC between its many users. A user is said to be electromagnetically compatible provided it satisfies three criteria: (1) it does not cause interference with other users, (2) it is not susceptible to emissions from other users, and (3) it does not cause interference with itself. Central to the goal of EMC is the concept of orthogonality between the users as determined by how cells are assigned in the multi-dimensional RF resource space.

However, perfect orthogonality between users is unlikely to be achieved in typical real world applications. For example, in the spatial dimension it is possible to design the main beams of transmit and receive antennas such that they do not overlap in specified directions. However, all antenna patterns include sidelobes which do overlap. Analogous statements apply to frequency domain spectra. These overlaps can lead to severe interference when a high power emitter, such as a radar, is co-located near a highly sensitive digital receiver, such as a wireless device. In the polarization domain, orthogonality

between users can be compromised by multiple reflections. As another example, the nonlinearities present in all electronic systems can generate unintended consequences for users of the RF resource space. Thus, a frequency hopping spread spectrum system produces a complicated pattern of harmonics, intermodulation products, and spurious responses that may cause problems for users in both nearby and distant frequency-domain cells of the RF resource space. In addition, the various domains of the resource space are all interrelated, as predicted by Maxwell's equations and Fourier analysis. Therefore, orthogonality in one domain can lead to undesired results in another. For example, shorter duration times for pulses in a time-division multiple access scheme causes wider frequency spectra that could be troublesome to some of the users.

In the present context, perfect orthogonality between users is referred to as strict orthogonality. Orthogonality that is intended, but not strictly achieved, is referred to as loose orthogonality. EMC applies automatically to those users for which strict orthogonality exists. On the other hand, EMC may or may not apply to those users for which there is loose orthogonality. Loose orthogonality is not necessarily to be avoided. In the following paragraphs a scheme is devised, which is briefly described where loose orthogonality is employed in order to increase the number of users in a CDMA direct sequence spread spectrum (DSSS) system.

CDMA DSSS Example

Consider a CDMA DSSS system for which all users have the same chip rate, R_c , data rate, R_b , and carrier frequency, f_0 , but are assigned different spreading codes which are nearly orthogonal. The chip rate is chosen such that the power spectral density (psd) of each user fills the common frequency band centered at f_0 having bandwidth, B_0 . This scheme is illustrated in Figure 3a where all users have identical power spectral densities and a maximum processing gain given by $L_0 = B_0/B_b$ where B_b is the data signal bandwidth. Because the codes are nearly orthogonal, a residual component due to each undesired signal exists at the correlator output of each receiver and limits the total number of users in the band to K_0 such that a pre-specified probability of error, P_e , is achieved. Because each DSSS signal has the maximum possible processing gain, it might be

conjectured that the number of DCMA DSSS users for the given frequency band and probability of error cannot exceed K_0 .

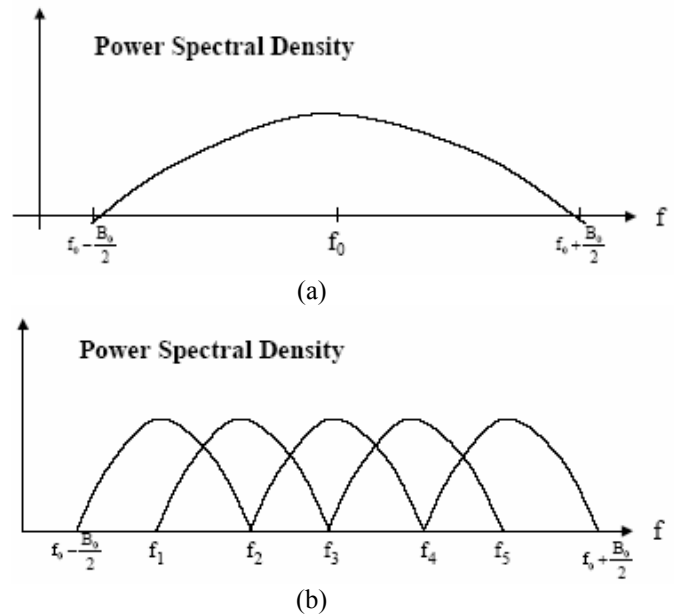


Figure 3: PSD of (a) Each CDMA DSSS System and (b) Subdivision of Original Frequency Band.

However, consider the scheme illustrated in Figure 3b where the original frequency band has been subdivided into 5 sub-bands. The center frequency bandwidth B_0 has been subdivided into 5 sub-bands, where each sub-band is given by

$$\begin{aligned} f_1 &= f_0 - B_0/3, & f_3 &= f_0 & f_5 &= f_0 + B_0/3 \\ f_2 &= f_0 - B_0/6, & f_4 &= f_0 + B_0/6 \end{aligned} \quad (1)$$

Let K_k , $k = 1, 2, \dots, 5$, denote the number of CDMA DSSS users in each sub-band where K_k is maximized such that the probability of error for each user does not exceed that of the scheme in Figure 3a. It has been shown both by analysis and computer simulation that the total number of users for the scheme of Figure 3b, given by

$$K = K_1 + K_2 + K_3 + K_4 + K_5 \quad (2)$$

is approximately 20 percent larger than K_0 . This result is partly explained by the loose orthogonality that exist between the overlapping sub-bands of Figure 3b (Note that the peak of one sub-band is placed at the null of the neighboring sub-band).

Also, the loose orthogonality of the spreading codes allows for more different codes of a fixed length to be generated that would be possible if strict orthogonality was enforced.

Nonetheless, loose orthogonality may result in EMI which reduces the quality of service (QoS) required by one or more users of the RF resource space. Consequently, the approaches for joint optimization of the multiple orthogonalizing transmission parameters should be constrained by EMC considerations. Assignments that are likely to cause unacceptable losses in QoS can then be removed from consideration.

For this purpose, users of the RF resource space having potential for undesired signal coupling can be identified. These can be divided into sets of emitter and receptor ports having specified coupling paths. It is assumed that one or more emitters can couple to a given receptor while a given emitter can couple to one or more receptors. Using the resource space dimensions, multidimensional profiles are established for each emitter and receptor port. These are used, along with characterizations of the coupling paths, to determine whether or not the power from unintentional users at each receptor port exceeds the susceptibility threshold for that port. Because of the complexity of the above approach, simple *rules of thumb* can be used to demonstrate the EMC constrained joint optimization procedure. These can then be refined so as to yield more accurate predictions.

These EMC considerations can be embedded in the system so that users who are assigned particular coordinates are not prevented from operating at acceptable levels of performance.

Exploiting Diversity and Applying Joint Transforms

The current *TH* concept incorporates the above considerations including the design of novel diverse waveforms to address the dilemma of increasing demand for improved performance of future communication and radar systems that will be co-located. Recent advances in hardware technology make it possible to design waveforms in real time that maximize signal-to-interference ratios, improve resolution, and increase information transfer.

For instance, temporal and spatial waveform diversity can support: reliable communications in realistic multipath environments, radar with multiple mission (tracking and imaging capability), interferometric radar and communications for better resolution and throughput, multistatic radar for improved discrimination, as well as integrated radar and communications in severe interference environments.

Also, joint time-frequency analysis (JTFA) has potential for the investigation of EMI/C problems in support of the *TH* approach. JTFA can be used to gain more insight and information than can be obtained from only a time-domain waveform or its frequency-domain counterpart. Time-frequency distributions are highly useful schemes for interference excision in spread spectrum communications systems, so their importance cannot be overlooked. Although JTFA is generally an effective approach, its applicability is limited in this case. In particular, the dimensionality would need to be extended to address solutions for joint optimization of an *n*-tuple space problem. This technique has not been fully exploited in the present concept design and is left for future research.

COMPUTER MODELING AND EMI ANALYSIS APPROACH

A computer model was generated for the case of 100 spatially fixed nodes (radio transceiver antennas) distributed uniformly over earth ground. This model was analyzed to assess the efficacy of selected optimization measures to enhance RF communications throughput and the potential for frequency reuse. Two ground propagation models were considered: (i) one based on a classical high-frequency ray tracing and diffraction formulation, which incorporates a lossy smooth earth model that accounts for signal fading as a function of frequency, distance, and surface propagation media effects [11, 12]; and (ii) an analytical model based on the Hata empirical formulation [13], which includes an average loss term to account for urban/terrain attenuation effects.

First, a baseline legacy system model was constructed consisting of a group of RF antenna systems each with identical transmitter and receiver operating characteristics and omni directional antenna patterns. All the antennas

were tuned to 2.4 GHz in the model. Electromagnetic coupling was computed for all possible pairs of interactions over each time slice. A successful transmission was assumed when a message packet was sent and received between an intended pair of nodes. This was accomplished on the basis of a single node-pair intentionally communicating with each other during a given time slice in the legacy system case. In the legacy system, only one pair of transmit-receive antennas could operate interference free (simultaneous transmissions were not considered viable as this could lead to significant interference in the legacy case). The total number of time slots over all possible time slots based on single-pair interactions for the legacy system was computed to be 9,900.

The next step was to introduce several additional RF resource space dimensions into the problem; namely, power range, beamwidth, smart antenna beam directionality and limited frequency agility. The results of analyzing changes in these other dimensions of the problem were then compared to the legacy system results in order to compute the effective improvement in data throughput and frequency reuse. In the augmented problem, the 3-dB beamwidths for each antenna were specified to be 12.5 degrees each with a Gaussian beam distribution in azimuth and elevation along their (coincident) boresight direction. The transmit and receive beams were aligned with respect to each other and then coupling interactions were recomputed for antenna pairs over each possible time slice. This is illustrated in Figure 4. In this case, multiple antennas were allowed to transmit and receive simultaneously. Intended pairs (RF links) were established in the presence of ambient interference due to unintentional signals from other antennas in the model. In addition, power control was employed to set the transmit power levels to threshold the intended receiver based on a predefined +10 dB SINR value. Information was then accumulated on the number of interference-free RF links and time slots in order to arrive at a throughput enhancement figure of merit.

By comparing the number of interference-free time slots involving simultaneous transmissions to the total number of time slots in the legacy case, approximately a 22X+ improvement in frequency reuse over the legacy system was predicted (or more than 450 simultaneous transmissions can take place). This was based primarily on

employing beam diversity, power control, and other geo-spatial diversity techniques. When frequency diversity is considered in addition to other control schemes, further improvement by nearly 38X+ over the legacy system was predicted. If modulation diversity as well as other waveform diversity schemes were to be employed, the improvement could be extended to nearly an order of magnitude above the legacy system.

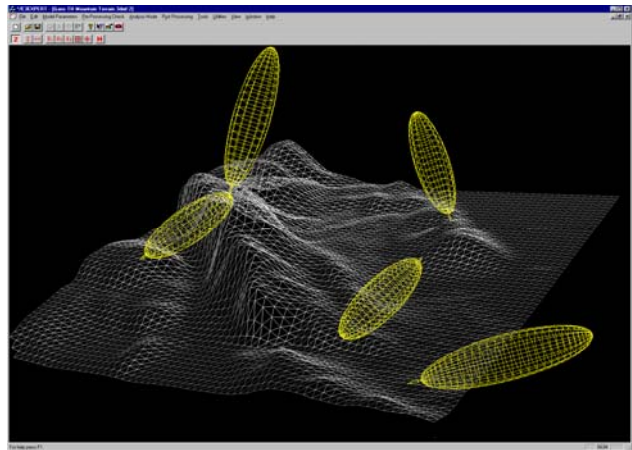


Figure 4: Earth Ground Computational Model Showing Spatial Beam Patterns.

Computational Optimization

Using only a subset of dimensions and assuming a relatively simple set of problem conditions, we observed that significant improvements in throughput and frequency reuse could be achieved by employing fairly straightforward diversity measures. These measures reflect the process of automatically optimizing certain parameters in the problem to improve communications performance, albeit, a number of simplified assumptions were made with regard to the availability of smart antenna technologies, stable broadband antenna performance, and so forth.

Perhaps an equally important result was that a viable approach had been demonstrated for efficiently computing EM coupling and associated figures of merit for decision making in near real time. For instance, on a PC with nearly 1 GB memory and a processor speed on the order of 2 GHz, it took well under a minute (and in most cases, just a few seconds) to analyze the 100-node configuration for interference and to verify what RF links were viable. The coupling models

that were used to analyze the problem over the iteration sample space and matrix of possibilities were based on conservative, discrete, closed-form analytical formulations. Hence, it was not too surprising that the computation times were relatively short. Nonetheless, it is believed that a scenario-based and rule-driven number-crunching capability would be highly useful as part of a *TH*-enabled system approach for real time environmental monitoring and management.

It should also be mentioned that some numerical modeling was performed on limited segments of the model to resolve uncertainty areas in the predicted results and to gain additional insights into the physics underlying the interference problem. This involved the use of hybrid moment method (MoM) and uniform theory of diffraction (UTD) techniques to analyze certain localized, near-field effects. It goes without saying that relying on a numerical solution as part of the *TH* system-level approach is impractical based on inherent limitations in today's computer technologies, but computational electromagnetics (CEM) can be used as an offline approach to studying methods for optimizing the problem.

One potential solution in overcoming the computational bottlenecks of CEM tools and techniques as part of a system-level *TH* approach in the future, will likely be to exploit novel parallel processing architectures and use of floating point gate array (FPGA) hardware. Indeed, upcoming multifunctional radio and sensor systems are already making more use of on-board memory and FPGA hardware to support distributed and accelerated space-time adaptive processing of data to meet real time performance goals.

ADDITIONAL CONSIDERATIONS

The above discussion on optimization for efficient utilization of the RF Transmission Hyperspace focused more on the methods to assign the dimensions of the RF resource space to meet a generalized set of performance objectives (e.g., maximizing frequency reuse). However, one can also exploit other aspects of the problem. For instance, methods to leverage the technology base in microelectronics with new waveforms and routing protocols—from the *medium access and control (MAC) layer* through the *network layer*—to construct an integrated system, can be leveraged to fully achieve the goals of multiobjective joint

optimization and to assure point-to-point connectivity. The multiobjective optimization is aimed at assuring optimum information pathways or the best routing scheme using a centralized or a distributed *TH*-enabled resource management hub (broker), implemented in either a fixed or mobile network mode. The goal is to develop, integrate, and evaluate the technology to enable equipment to automatically select spectrum and operating modes to both minimize disruption of existing users and to ensure operation of information and sensor systems. This will require the development of new *appliqués* and an intelligent centralized or distributed architecture for legacy and future emitter systems for joint service utility. Both the enabling technologies and system concepts must be developed to provide assured military communications in support of worldwide, short notice deployments through the dynamic redistribution of allocated spectrum.

The initial implementation of the *TH* concept will likely be realized by enabling legacy and upcoming software defined radio systems in development, as well as emerging wideband technologies. In this scheme, the new *appliqué* and any necessary constraints (based on approved spectrum policies, protocols, case studies, and lessons learned) could be applied to a selected technology or device e.g., the Joint Tactical Radio System (JTRS) for managing the RF resource space and network routing schemes for fixed-frequency and frequency-agile systems, and for both static and mobile scenarios. The application of approved spectrum management policy constraints and protocols is critical to the automated decision-making process embedded within the *TH*-enabled technology.

CONCLUSION

This article described a new “spectrum management” paradigm that can be characterized as a *jointly optimized transmission space*. In this approach algorithmic techniques are used to mathematically perform joint optimization of frequency, time, space, code/modulation, polarization, and other signal dimensions to ensure orthogonality and allow for multiple users to operate without interference. This approach is embodied in the *Transmission Hyperspace (TH)* concept and is intended to be a unifying visionary solution to today's problem of achieving efficient spectrum management that leverages techniques

for selectively maximizing desired RF communications links and by denying unwanted links in the presence of EM jamming environments. To accomplish this, a computationally-efficient method of analyzing the potentially large matrix of coupling interactions was developed and demonstrated that could provide a foundation for an embedded near real time environmental monitoring and interference analysis component. However, more research needs to be conducted to find ways of further optimizing the computational approach. This may involve investigations of how scalable CEM tools can be integrated within the system architecture. This is only one of the many challenges that are being addressed in the future.

The TH concept supports the notion of spectrum management for *systems of systems* of transmitters and receivers on virtually any scale. TH-enabled systems will lead to increased channel capacity, information throughput, and communications range as well as influence the generation of new policies and a more efficient methodology for spectrum management that could be applied at various levels of an overall communications network or multisensor grid.

Acknowledgements

The authors wish to acknowledge the support of Dr. Michael Gans of the Air Force Research Laboratory/IFGC, Rome Research Site and Dr. Alan Lindsey (formerly of AFRL/IFGC, RRS) for their support in various aspects of this research provided under Contract No. FA8750-04-C-0028.

References

- [1] M. R. Garey and D. S. Johnson. *Computers and Intractability: A Guide to the Theory of NP-Completeness*. Freeman, New York, (1979).
- [2] Kirkpatrick, S., C. D. Gelatt Jr., M. P. Vecchi, "Optimization by Simulated Annealing", *Science*, 220, 4598, 671-680, 1983.
- [3] Glover F., "Tabu Search: A Tutorial", *Interfaces*, 20(4):74-94, (1990).

- [4] D. E. Goldberg. *Genetic Algorithms in Search, Optimization, and Machine Learning*. Addison-Wesley, Reading, Massachusetts, (1989).
- [5] C. K. Mohan, A Framework for Evolutionary Operators, *International Journal of Smart Engineering System Design*, 1(3):1-38, (1998).
- [6] D. B. Fogel (1995) "Evolutionary Computation: Toward a New Philosophy of Machine Intelligence," IEEE Press, Piscataway, NJ.
- [7] Rechenberg, I. (1973) "Evolutionsstrategie: Optimierung technischer Systeme nach Prinzipien der biologischen Evolution", Stuttgart: Fromman-Holzboog.
- [8] K. Veeramachaneni, T. Peram, C. Mohan and L. Osadciw, Optimization using Particle Swarms with Near Neighbor Interactions, in *Proc. Genetic and Evolutionary Computation Conference (GECCO)*, Chicago, July 2003.
- [9] I. Das. *Nonlinear Multicriteria Optimization and Robust Optimality*. Ph.D. Thesis (1997), Dept. of Computational and Applied Mathematics, Rice University, Houston, TX 77251, USA.
- [10] I. Das and J. E. Dennis. *Normal-Boundary Intersection: An Alternate Approach for Generating Pareto-optimal Points in Multicriteria Optimization Problems*. ICASE-NASA Tech. Report 96-62, July 1996.
- [11] T. S. Rappaport, R. Muhamed, V. Kapoor & J. D. Gibson, Ed., "*The Mobile Communications Handbook*," CRC Press, FL, Chap. 22, pp. 357-365, 1996.
- [12] T. S. Rappaport, "*Wireless Communications Principles & Practices*," Prentice Hall, NJ, Chap. 3, pp. 119-120, 1996.
- [13] "*Spectrum Planning Report: Investigation of Modified Hata Propagation Models*," Spectrum Planning Team, Radio Frequency Planning Group and Australian Communications Authority, Document: SP 2/01, April 2001.

A Review of the Path Integral Time Domain Method

Jeffrey A. Miller, Ph.D.

Abstract

The path integral time domain method (PITD) is a relatively new numerical technique for electromagnetic scattering, propagation, and transmission line analysis. The underlying theory and numerical technique are demonstrated and several one-dimensional problems illustrate the interesting properties of the method

Introduction

The path integral time-domain method as introduced by Nevels[1] has several intriguing properties. These include the collocation of the electric and magnetic fields, the absence of numerical dispersion, and the spatial domain sampling at the Nyquist limit. This paper will review the theory and numerical procedure of the path integral time domain method. One-dimensional examples illustrate the most practical applications of the method at its current state of development.

Maxwell's Equations

Maxwell's time dependent equations for a source free region are given by

$$\nabla \times \mathbf{H} = \sigma \cdot \mathbf{E} + \varepsilon \cdot \frac{\partial \mathbf{E}}{\partial t} \quad (1)$$

$$\nabla \times \mathbf{E} = -\rho \cdot \mathbf{H} - \mu \cdot \frac{\partial \mathbf{H}}{\partial t} \quad (2)$$

where σ and ρ are the electric and magnetic(fictitious) conductivities, and \mathbf{E} and \mathbf{H} are the electric and magnetic field intensities. Throughout this paper vector quantities are denoted by bold face type. The permittivity ε and permeability μ of the medium are real numbers that are time independent. Combining the two curl equations into a single vector equation leads to

$$\frac{\partial \mathbf{F}}{\partial t} = \bar{\mathbf{S}} \cdot \mathbf{F} \quad (3)$$

by isolating the time derivatives on the left hand side and creating a new vector

$$\mathbf{F}^T = [E_x \quad E_y \quad E_z \quad H_x \quad H_y \quad H_z] \text{ and the matrix} \quad (4)$$
$$\bar{\mathbf{S}} = \begin{bmatrix} -\sigma/\varepsilon & \varepsilon^{-1} \cdot \nabla \times \\ -\mu^{-1} \cdot \nabla \times & -\rho/\mu \end{bmatrix}$$

The Propagator

The propagator plays a significant role in the PITD method. As will be shown, the propagator is the mechanism by which fields are advanced in time and propagated in space. Barton [2] states that a propagator $\bar{\mathbf{K}}$ is found by solving equation (3), which is a vector hyperbolic equation, substituting $\bar{\mathbf{K}}$ for \mathbf{F} as in equation (5) and adding the initial condition shown in equation (6).

$$\frac{\partial \bar{\mathbf{K}}}{\partial t} = \bar{\mathbf{S}} \cdot \bar{\mathbf{K}} \quad (5)$$

$$\lim_{t \rightarrow t'} \bar{\mathbf{K}}(\mathbf{r}, \mathbf{r}'; t, t') = \bar{\mathbf{I}} \delta(\mathbf{r} - \mathbf{r}') \quad (6)$$

In equation (6), $\bar{\mathbf{I}}$ is the identity matrix, $\delta(\mathbf{r} - \mathbf{r}')$ is the Dirac delta function, t, t' are the current and initial times, and the vectors \mathbf{r}, \mathbf{r}' represent the current and initial spatial locations respectively. In Cartesian coordinates, $\mathbf{r} = x\hat{\mathbf{x}} + y\hat{\mathbf{y}} + z\hat{\mathbf{z}}$ where unit vectors are denoted by bold face type with hats. The initial vector is likewise $\mathbf{r}' = x'\hat{\mathbf{x}} + y'\hat{\mathbf{y}} + z'\hat{\mathbf{z}}$. By straightforward substitution a solution to (5) is

$$\bar{\mathbf{K}} = e^{\bar{\mathbf{S}}t} \bar{\mathbf{K}}_0. \quad (7)$$

Using the initial condition (6) with (7), leads to

$$\bar{\mathbf{K}}_0 = e^{-\bar{\mathbf{S}}t'} \bar{\mathbf{I}} \delta(\mathbf{r} - \mathbf{r}'). \quad (8)$$

Substituting (8) into (7) gives the final form of the propagator as

$$\bar{\mathbf{K}} = e^{\bar{\mathbf{S}}(t)} e^{\bar{\mathbf{S}}(-t')} \bar{\mathbf{I}} \delta(\mathbf{r} - \mathbf{r}') = e^{\bar{\mathbf{S}}(\tau)} \bar{\mathbf{I}} \delta(\mathbf{r} - \mathbf{r}'). \quad (9)$$

Finally, the delta function in (9) is replaced with its spatial inverse Fourier transform representation

$$\delta(\mathbf{r} - \mathbf{r}') = \int_{-\infty}^{\infty} e^{j2\pi \mathbf{k} \cdot (\mathbf{r} - \mathbf{r}')} d\mathbf{k} \quad (10)$$

giving

$$\bar{\mathbf{K}}(\mathbf{r}, \mathbf{r}'; \tau) = e^{\bar{\mathbf{S}}\tau} \bar{\mathbf{I}} \int_{-\infty}^{\infty} e^{j2\pi \mathbf{k} \cdot (\mathbf{r} - \mathbf{r}')} d\mathbf{k}. \quad (11)$$

Equation (11) doesn't appear to simplify the expression for the propagator but with a little linear algebra, a new propagator matrix that is more beneficial is obtained. The $\bar{\mathbf{S}}$ matrix for a simple inhomogeneous, isotropic medium in three-dimensional Cartesian coordinates is

$$\bar{\mathbf{S}} = \begin{bmatrix} -\sigma/\varepsilon & 0 & 0 & 0 & -(1/\varepsilon)\partial_z & (1/\varepsilon)\partial_y \\ 0 & -\sigma/\varepsilon & 0 & (1/\varepsilon)\partial_z & 0 & -(1/\varepsilon)\partial_x \\ 0 & 0 & -\sigma/\varepsilon & -(1/\varepsilon)\partial_y & (1/\varepsilon)\partial_x & 0 \\ 0 & (1/\mu)\partial_z & -(1/\mu)\partial_y & -\rho/\mu & 0 & 0 \\ -(1/\mu)\partial_z & 0 & (1/\mu)\partial_x & 0 & -\rho/\mu & 0 \\ (1/\mu)\partial_y & -(1/\mu)\partial_x & 0 & 0 & 0 & -\rho/\mu \end{bmatrix}. \quad (12)$$

In (12), ∂_i indicates a partial derivative with respect to the subscript. Notice that the matrix $\bar{\mathbf{S}}$ is an operator matrix that operates on \mathbf{r} but not on \mathbf{k} . Therefore, move the exponential with the matrix $\bar{\mathbf{S}}$ under the integral sign where it operates on $\exp(j2\pi \mathbf{k} \cdot \mathbf{r})$ with the result that the partial derivatives are replaced with the components of \mathbf{k} as seen in (13).

$$\partial_x \rightarrow j2\pi k_x \quad \partial_y \rightarrow j2\pi k_y \quad \partial_z \rightarrow j2\pi k_z \quad (13)$$

The new form of $\bar{\mathbf{S}}(\mathbf{r}, \mathbf{k})$ is

$$\bar{\mathbf{S}}(\mathbf{r}, \mathbf{k}) = \begin{bmatrix} -\sigma/\varepsilon & 0 & 0 & 0 & \frac{-j2\pi k_z}{\varepsilon} & \frac{j2\pi k_y}{\varepsilon} \\ 0 & -\sigma/\varepsilon & 0 & \frac{j2\pi k_z}{\varepsilon} & 0 & \frac{-j2\pi k_x}{\varepsilon} \\ 0 & 0 & -\sigma/\varepsilon & \frac{-j2\pi k_y}{\varepsilon} & \frac{j2\pi k_x}{\varepsilon} & 0 \\ 0 & \frac{j2\pi k_z}{\mu} & \frac{-j2\pi k_y}{\mu} & -\rho/\mu & 0 & 0 \\ \frac{-j2\pi k_z}{\mu} & 0 & \frac{j2\pi k_x}{\mu} & 0 & -\rho/\mu & 0 \\ \frac{j2\pi k_y}{\mu} & \frac{-j2\pi k_x}{\mu} & 0 & 0 & 0 & -\rho/\mu \end{bmatrix}. \quad (14)$$

Matrix $\bar{\mathbf{S}}(\mathbf{r}, \mathbf{k})$ is shown as a function of \mathbf{r} as the material parameters $(\mu, \varepsilon, \sigma, \rho)$ vary with position. The propagator becomes

$$\bar{\mathbf{K}}(\mathbf{r}, \mathbf{r}'; \tau) = \int_{-\infty}^{\infty} e^{\bar{\mathbf{S}}(\mathbf{r}, \mathbf{k})\tau} e^{j2\pi \mathbf{k} \cdot (\mathbf{r} - \mathbf{r}')} d\mathbf{k}. \quad (15)$$

Readers familiar with state space techniques will realize that the exponential of $\bar{\mathbf{S}}(\mathbf{r}, \mathbf{k})\tau$ is changed into a state transition matrix (fundamental matrix in many mathematical texts) by several techniques (DeRusso, *et al.* [3] and Wiberg [4]). The eigenvalue approach is discussed. The eigenvalues and eigenvectors of $\bar{\mathbf{S}}(\mathbf{r}, \mathbf{k})$ are sought. A modal matrix $\bar{\mathbf{M}}$ is a column-oriented compilation of the eigenvectors. The state transition matrix $\bar{\mathbf{A}}$ is

$$\bar{\mathbf{A}} = \bar{\mathbf{M}} \mathbf{P}(\lambda_i \tau) \bar{\mathbf{M}}^{-1} \quad (16)$$

where $\mathbf{P}(\lambda_i \tau)$ is a diagonal matrix with the eigenvalues of $\bar{\mathbf{S}}(\mathbf{r}, \mathbf{k})$ multiplied by τ . The eigenvalues and eigenvectors are aligned such that the eigenvector in the first column of the modal matrix corresponds to the eigenvalue located in the first diagonal element. The second column of the modal matrix is another eigenvector and its associated eigenvalue is the second term in the diagonal matrix. This pattern is repeated for each eigenvalue-eigenvector pair. The inverse of the modal matrix $\bar{\mathbf{M}}^{-1}$ is the last term on the right hand side of (16). The propagator takes the simple form

$$\bar{\mathbf{K}}(\mathbf{r}, \mathbf{r}'; \tau) = \int_{-\infty}^{\infty} \bar{\mathbf{A}} e^{j2\pi \mathbf{k} \cdot (\mathbf{r} - \mathbf{r}')} d\mathbf{k} \quad (17)$$

where, for example, in a lossless $(\sigma \rightarrow 0, \rho \rightarrow 0)$ region $\bar{\mathbf{A}}$ is

$$\bar{\mathbf{A}} = \begin{bmatrix} a_{11} & a_{12} & a_{13} & a_{14} & a_{15} & a_{16} \\ a_{21} & a_{22} & a_{23} & a_{24} & a_{25} & a_{26} \\ a_{31} & a_{32} & a_{33} & a_{34} & a_{35} & a_{36} \\ a_{41} & a_{42} & a_{43} & a_{44} & a_{45} & a_{46} \\ a_{51} & a_{52} & a_{53} & a_{54} & a_{55} & a_{56} \\ a_{61} & a_{62} & a_{63} & a_{64} & a_{65} & a_{66} \end{bmatrix} \quad (18)$$

with

$$\begin{aligned} a_{11} &= a_{44} = \left[k_x^2 + (k_y^2 + k_z^2) \cos(u) \right] / k^2 \\ a_{12} &= a_{21} = a_{45} = a_{54} = k_x k_y (1 - \cos(u)) / k^2 \\ a_{13} &= a_{31} = a_{46} = a_{64} = k_x k_z (1 - \cos(u)) / k^2 \\ a_{14} &= a_{25} = a_{36} = a_{41} = a_{52} = a_{63} = 0 \\ a_{15} &= -a_{24} = -j\eta k_z \sin(u) / k \\ a_{16} &= -a_{34} = j\eta k_y \sin(u) / k \\ a_{22} &= a_{55} = \left[k_y^2 + (k_x^2 + k_z^2) \cos(u) \right] / k^2 \\ a_{23} &= a_{32} = a_{56} = a_{65} = k_y k_z (1 - \cos(u)) / k^2 \\ a_{26} &= -a_{35} = -j\eta k_x \sin(u) / k \\ a_{33} &= a_{66} = \left[k_z^2 + (k_x^2 + k_y^2) \cos(u) \right] / k^2 \\ a_{42} &= -a_{51} = jk_z \sin(u) / \eta k \\ a_{43} &= -a_{61} = -jk_y \sin(u) / \eta k \\ a_{53} &= -a_{62} = jk_x \sin(u) / \eta k \end{aligned}, \quad (19)$$

$$u = 2\pi k v_p \tau \text{ and } k^2 = k_x^2 + k_y^2 + k_z^2.$$

The Path Integral for Electromagnetic Scattering

Barton [2] writes that once the propagator is known an initial field distribution \mathbf{F}_0 is propagated a single time step by

$$\mathbf{F}(\mathbf{r}, t) = \int_{-\infty}^{\infty} \bar{\mathbf{K}}(\mathbf{r}, \mathbf{r}'; \tau) \mathbf{F}_0(\mathbf{r}', t') d\mathbf{r}'. \quad (20)$$

Putting equation (17) into equation (20) gives

$$\mathbf{F}(\mathbf{r}, t) = \int_{-\infty}^{\infty} \int_{-\infty}^{\infty} \bar{\mathbf{A}} e^{j2\pi \mathbf{k} \cdot (\mathbf{r} - \mathbf{r}')} d\mathbf{k} \mathbf{F}_0(\mathbf{r}', t') d\mathbf{r}'. \quad (21)$$

Since $\mathbf{F}_0(\mathbf{r}', t')$ is not a function of \mathbf{k} , $\bar{\mathbf{A}}$ and $\exp(j2\pi \mathbf{k} \cdot \mathbf{r})$ are not functions of the initial spatial vector \mathbf{r}' , equation (21) is after reversing the order of integration

$$\mathbf{F}(\mathbf{r}, t) = \int_{-\infty}^{\infty} \int_{-\infty}^{\infty} \bar{\mathbf{A}} \mathbf{F}_0(\mathbf{r}', t') e^{j2\pi\mathbf{k}\cdot\mathbf{r}} e^{-j2\pi\mathbf{k}\cdot\mathbf{r}'} d\mathbf{r}' d\mathbf{k}. \quad (22)$$

Equation (22) reveals significant insight into the operation of this method. Moving $\bar{\mathbf{A}}$ and $\exp(j2\pi\mathbf{k}\cdot\mathbf{r})$ outside of the internal integral

$$\mathbf{F}(\mathbf{r}, t) = \int_{-\infty}^{\infty} \bar{\mathbf{A}} \left\{ \int_{-\infty}^{\infty} \mathbf{F}_0(\mathbf{r}', t') e^{-j2\pi\mathbf{k}\cdot\mathbf{r}'} d\mathbf{r}' \right\} e^{j2\pi\mathbf{k}\cdot\mathbf{r}} d\mathbf{k}. \quad (23)$$

Equation (23) is a remarkable and exciting equation! The initial field distribution is Fourier transformed into the spectral domain, multiplied by the transition matrix and inverse Fourier transformed back to the time-space domain. This current spatial distribution then becomes the initial field for the next time step. Assuming that τ is some small incremental element of time and $t = N\tau + t_0$, a time evolving picture of the electromagnetic field distribution is obtained by repeated application of equation (23)

$$\mathbf{F}(\mathbf{r}, t) = \mathcal{F}^{-1} \left\{ \bar{\mathbf{A}}_N \mathcal{F} \left\{ \mathcal{F}^{-1} \left\{ \bar{\mathbf{A}}_{N-1} \dots \mathcal{F} \left\{ \mathcal{F}^{-1} \left\{ \bar{\mathbf{A}}_1 \mathcal{F} \left\{ \mathbf{F}_0(\mathbf{r}', t_0) \right\} \right\} \dots \right\} \right\} \right\} \right\}. \quad (24)$$

Equation (24) is a symbolic representation of the path integral for electromagnetic scattering. A careful observer might mention that (24) has successive operations of inverse and forward Fourier transforms that allows their removal. For a strictly homogeneous region, which is not very interesting in a practical sense, (24) reduces to a single forward transform of the initial field distribution, the transition matrix is then applied N times, and a single inverse Fourier transform gives the final field distribution

$$\mathbf{F}(\mathbf{r}, t) = \mathcal{F}^{-1} \left\{ \bar{\mathbf{A}}_N \left\{ \bar{\mathbf{A}}_{N-1} \dots \left\{ \bar{\mathbf{A}}_1 \mathcal{F} \left\{ \mathbf{F}_0(\mathbf{r}', t_0) \right\} \right\} \dots \right\} \right\}. \quad (25)$$

In a general inhomogeneous space, the above statement and equation is *not true* because the transition matrix is a function of \mathbf{r} .

Numerical Method

Examining a single time step (23), it is apparent that Fourier transforms are an important aspect of this method. Ziemer, *et al.* [5] state that a bandwidth limited signal having no frequency components above a certain frequency f_h is completely specified by samples taken at a uniform rate greater than $2f_h$ which is known as the Nyquist limit. As a minimum, a numerical space is sampled at twice the rate of the highest frequency of interest. For example, if the highest frequency of interest is 3 GHz, then the minimum spatial sampling is 0.05 meters between samples assuming the phase velocity in the medium is 3×10^8 m/s. Since the continuous space is now a discretely sampled numerical space, the Fourier transforms are performed by discrete equivalents (Press, *et al.* [6])

$$X(n_i \Delta \mathbf{k}) = \sum_{m_i=0}^{N_i-1} x(m_i \Delta \mathbf{r}) e^{-j2\pi n_i m_i / N_i} \quad (26)$$

$$x(m_i \Delta \mathbf{r}) = \frac{1}{N_i} \sum_{n_i=0}^{N_i-1} X(n_i \Delta \mathbf{k}) e^{j2\pi n_i m_i / N_i} \quad (27)$$

where the i subscript indicates multidimensional capacity. For example, (26) for a two dimensional transform has a double summation. N_i is the total number of spatial samples in the i^{th} dimension. The spatial discretization yields a spectral domain with

$$\Delta k_i = \frac{1}{N_i \Delta r_i} \quad (28)$$

where Δr_i represents one of the spatial elements $\Delta x, \Delta y$, or Δz . The spectral frequencies take on both positive and negative values

$$n_i \Delta k_i \equiv \frac{n_i}{N_i \Delta r_i}, \quad n_i = -\frac{N_i}{2}, \dots, \frac{N_i}{2}. \quad (29)$$

Taking a single time step of (25) and including (26) and (27) leads to

$$\mathbf{F}(m_i \Delta \mathbf{r}, t) = \frac{1}{N_i} \sum_{n_i=0}^{N_i-1} \bar{\mathbf{A}}(m_i \Delta \mathbf{r}, n_i \Delta \mathbf{k}_i) \left\{ \sum_{p_i=0}^{N_i-1} \mathbf{F}(p_i \Delta \mathbf{r}, t') e^{-j \frac{2\pi n_i p_i}{N_i}} \right\} e^{j \frac{2\pi n_i m_i}{N_i}}. \quad (30)$$

Explicit in (30) is the dependence of the state transition matrix elements on the position \mathbf{r} of the field components. In an inhomogeneous space $\bar{\mathbf{A}}(\mathbf{r}, \mathbf{k})$ is allowed to change for every $\Delta \mathbf{r}$. A complete set of spectral components exists for each state transition matrix. Computational constraints of memory and speed determine if the elements are computed once and stored or computed on the fly. The electromagnetic field propagates in the numerical space by repeated applications of (30). It is important to reiterate here that all field components are collocated in space and time.

Single Dimension Problems

This section examines the PITD method for solutions of one-dimensional problems. These problems have plane wave fields and normal incidence. Numerical concerns about stability, numerical dispersion, and numerical error are addressed and an explicit form is introduced. Maxwell's equations for a single dimension lossless region are

$$\frac{\partial H_y}{\partial x} = \epsilon \frac{\partial E_z}{\partial t} \quad (31)$$

$$\frac{\partial E_z}{\partial x} = \mu \frac{\partial H_y}{\partial t} \quad (32)$$

where the material parameters are scalars and allowed to be functions of position x . The field components are selected and labeled to be consistent with the three-dimensional derivation. The x-

axis is the direction of propagation, the electric and magnetic field intensities are perpendicular to this direction and each other. Additionally, $k_x \equiv k$, the free space propagation constant, but the subscript will be retained. As before, rearrange (31) and (32) into a vector equation,

$$\frac{\partial}{\partial t} \begin{bmatrix} E_z \\ H_y \end{bmatrix} = \begin{bmatrix} 0 & \frac{1}{\epsilon} \frac{\partial}{\partial x} \\ \frac{1}{\mu} \frac{\partial}{\partial x} & 0 \end{bmatrix} \cdot \begin{bmatrix} E_z \\ H_y \end{bmatrix}. \quad (33)$$

The $\mathbf{S}(x, k_x)$ matrix is a 2 x 2, which using (13) and showing the positional dependency explicitly is

$$\bar{\mathbf{S}}(x, k_x) = \begin{bmatrix} 0 & \frac{j2\pi k_x}{\epsilon(x)} \\ \frac{j2\pi k_x}{\mu(x)} & 0 \end{bmatrix}. \quad (34)$$

The eigenvalue method finds the eigenvalues and eigenvectors of the $\bar{\mathbf{S}}(x, k_x)$ matrix in (34). Table 1 lists the two eigenvalues and their corresponding eigenvectors.

Table 1. Eigenvalues and eigenvectors for 1-D lossless materials

	Eigenvalue	Eigenvector
1	$j2\pi k_x v_p$	$\begin{bmatrix} 1 \\ 1/\eta \end{bmatrix}$
2	$-j2\pi k_x v_p$	$\begin{bmatrix} 1 \\ -1/\eta \end{bmatrix}$

Introducing the phase velocity $v_p = 1/\sqrt{\mu\epsilon}$ and intrinsic impedance $\eta = \sqrt{\mu/\epsilon}$ of the medium simplifies the equations. The state transition matrix derived from the eigenvalues and eigenvectors using (16) is

$$\bar{\mathbf{A}} = \begin{bmatrix} 1 & 1 \\ 1/\eta & -1/\eta \end{bmatrix} \begin{bmatrix} \exp(j2\pi k_x v_p \tau) & 0 \\ 0 & \exp(-j2\pi k_x v_p \tau) \end{bmatrix} \frac{1}{2} \begin{bmatrix} 1 & \eta \\ 1 & -\eta \end{bmatrix} \quad (35)$$

$$\bar{\mathbf{A}} = \begin{bmatrix} \cos(2\pi k_x v_p \tau) & j\eta \sin(2\pi k_x v_p \tau) \\ (j/\eta) \sin(2\pi k_x v_p \tau) & \cos(2\pi k_x v_p \tau) \end{bmatrix}. \quad (36)$$

Equation (36) is also called a rotation matrix (Nevels, *et al.* [7]) where the rotation angle is $\phi = 2\pi k_x v_p \tau$. The simplicity of this state transition matrix is exploited obtaining the explicit form of the PITD method in a later section. Equation (23), which represents a single time step or evolution of the fields, becomes

$$\begin{bmatrix} E_z(x,t) \\ H_y(x,t) \end{bmatrix} = \mathfrak{F}^{-1} \left\{ \begin{bmatrix} \cos(2\pi k_x v_p \tau) & j\eta \sin(2\pi k_x v_p \tau) \\ (j/\eta) \sin(2\pi k_x v_p \tau) & \cos(2\pi k_x v_p \tau) \end{bmatrix} \mathfrak{F} \left\{ \begin{bmatrix} E_z(x,t') \\ H_y(x,t') \end{bmatrix} \right\} \right\}. \quad (37)$$

Letting a Fourier transformed quantity be represented by a tilde over the quantity, (37) is

$$\begin{bmatrix} E_z(x,t) \\ H_y(x,t) \end{bmatrix} = \mathfrak{F}^{-1} \left\{ \begin{bmatrix} \cos(2\pi k_x v_p \tau) \tilde{E}_z(k_x, t') + j\eta \sin(2\pi k_x v_p \tau) \tilde{H}_y(k_x, t') \\ (j/\eta) \sin(2\pi k_x v_p \tau) \tilde{E}_z(k_x, t') + \cos(2\pi k_x v_p \tau) \tilde{H}_y(k_x, t') \end{bmatrix} \right\}. \quad (38)$$

Numerically equation (38) becomes

$$\begin{aligned} E_z(m\Delta x, t) &= \frac{1}{N} \sum_{n=0}^{N-1} \left(\cos(u) \tilde{E}_z(n\Delta k_x, t') + j\eta \sin(u) \tilde{H}_y(n\Delta k_x, t') \right) e^{j \frac{2\pi n m}{N}} \\ H_y(m\Delta x, t) &= \frac{1}{N} \sum_{n=0}^{N-1} \left((j/\eta) \sin(u) \tilde{E}_z(n\Delta k_x, t') + \cos(u) \tilde{H}_y(n\Delta k_x, t') \right) e^{j \frac{2\pi n m}{N}} \end{aligned} \quad (39)$$

where $u = 2\pi n \Delta k_x v_p \tau$.

Reflection from a Half Space

The geometry for the first example, reflection from a dielectric half space is in Figure 1. Standard Fourier transforms require a uniform discretization of the numerical space. The discretization chosen should provide at least two samples per wavelength in the dielectric region at the highest frequency of interest. The boundary between the two half spaces *is not* a sample point.

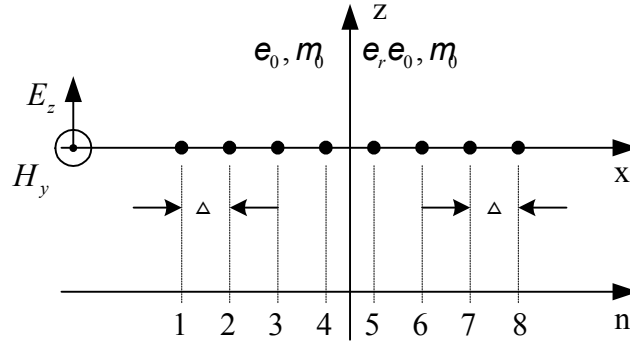


Figure 1. Reflection from a half space

The input source is a bandwidth limited Gaussian created at time zero by

$$E_z(n\Delta, t=0) = e^{-\left(\frac{n-pk}{\beta}\right)^2}, n \in \text{free space region} \quad (40)$$

where pk is the peak location of the Gaussian and β determines the bandwidth of the signal. The maximum input electric field is one volt per meter. Because the field components are collocated in both space and time, the magnetic field is simply the electric field divided by the intrinsic impedance.

Once the initial plane wave is placed in the numerical space the path integral is evaluated by:

1. Spatially Fourier transforming the field components $\mathbf{E}_z, \mathbf{H}_y$.
2. Inverse Fourier transforming the product of the state transition matrix and the data from step 1. Note that for two different material regions two state transition matrices exist and the correct one for each spatial point applies to (39).

$$E_z(m, t) = \frac{1}{N} \sum_{n=0}^{N-1} \left(\cos(u) \tilde{E}_z(n, t') + j\eta \sin(u) \tilde{H}_y(n, t') \right) e^{j \frac{2\pi n m}{N}} \quad (41)$$

$$H_y(m, t) = \frac{1}{N} \sum_{n=0}^{N-1} \left((j/\eta) \sin(u) \tilde{E}_z(n, t') + \cos(u) \tilde{H}_y(n, t') \right) e^{j \frac{2\pi n m}{N}} \quad (42)$$

Table 2. State transition matrices elements

	Region	
	Free Space	Dielectric
u	$2\pi n \Delta k_x c \tau$	$2\pi n \Delta k_x (c/\sqrt{\epsilon_r}) \tau$
u when $\tau = \Delta/c$	$2\pi n/N$	$2\pi n/N \sqrt{\epsilon_r}$

(41) and (42) the argument of the sinusoids depends on the region (see Table 2). The distance the field propagates in a single time step is a function of the time step (τ) and the phase velocity (v_p). In a homogeneous space, one has great flexibility in choosing the time step. The natural time step ($\tau = \Delta/v_p$) appears to be the best choice for an inhomogeneous space. For the example from Figure 1, the phase velocity chosen to calculate the time step is the speed of light in free space.

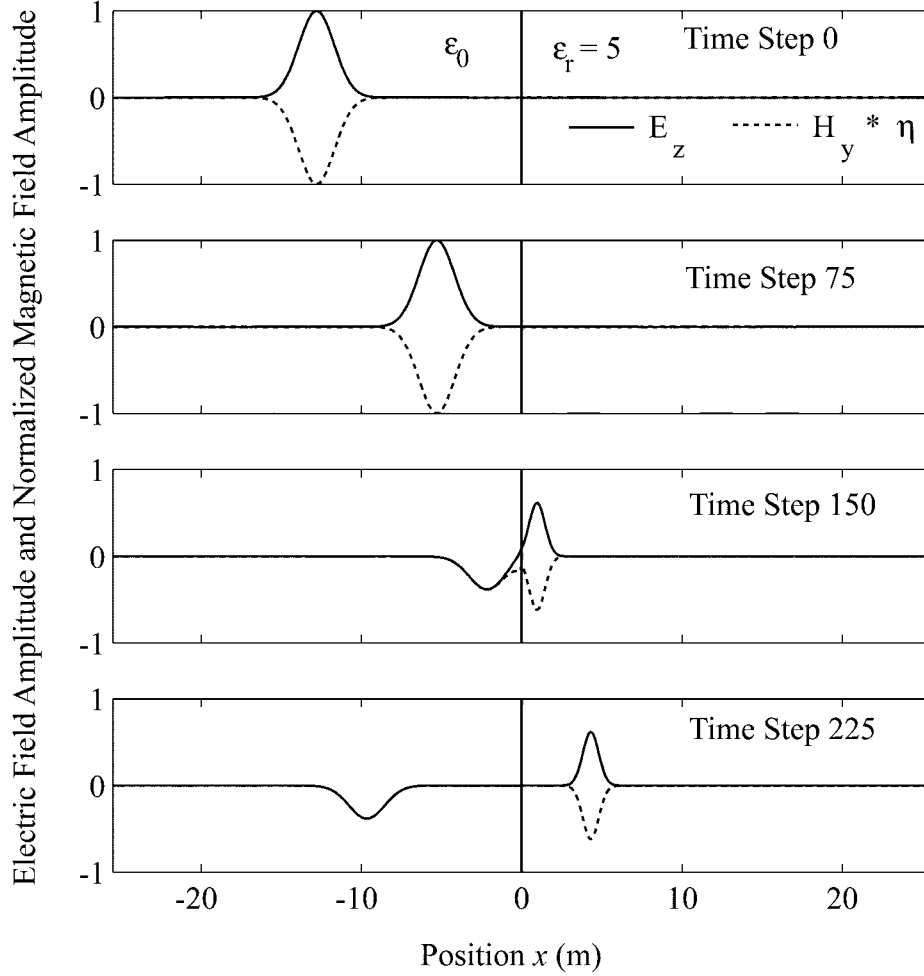


Figure 2. Reflection and transmission for a dielectric half space

Figure 2 is a series of time slices for a plane wave interacting with a dielectric half space. The intrinsic impedance in each region multiplies the magnetic field component to normalize it for display purposes. The numerical parameters for the simulation are in Table 3. The reflection coefficient is -0.382 and the transmission coefficient is 0.618 . At time step 225, the forward traveling wave has a maximum electric field of 0.619 V/m while the scattered wave has a minimum of -0.383 V/m. The percent error is 0.262% and 0.162% for the reflection coefficient and transmission coefficient, respectively. Single precision computer arithmetic gave this level of accuracy.

Table 3. Reflection and transmission from a half space

N	Δ	τ	ϵ_r	β
512	0.1 m	Δ/c	5	$7\sqrt{\epsilon_r}$

Kraus and Carver [8] define the energy density of a plane wave as

$$w = \frac{1}{2} \epsilon E^2 + \frac{1}{2} \mu H^2 . \quad (43)$$

The energy density in Table 4 shows the energy density in each of the half spaces as well as the total energy. Treating the time step 0 energy density as the true value, the percent error for the total energy density is 0.173% at time steps 150 and 225. It is somewhat surprising that the energy density is slightly greater after the incident field begins interacting with the lossless dielectric half space. Fortunately, the energy density doesn't continue to increase during additional time steps. The uncertainty of the physical boundary between the two regions produces the error in the energy density.

A comparison of the magnitude of the reflection coefficient between theoretical analysis and PITD method for a half space of changing permittivity is in Figure 3. A single spatial and time discretization is kept for all permittivity values. The spatial discretization meets the Nyquist requirement of two samples per wavelength in the highest permittivity dielectric at the highest frequency contained in the Gaussian input field. The PITD method agrees to within 0.3% the theoretical value of the reflection coefficient for all permittivities.

Table 4. Energy density for scattering from a dielectric half space

Time Step	Free Space	Dielectric $\epsilon_r = 5$	Total
0	0.1737×10^{-9}	0	0.1737×10^{-9}
75	0.1737×10^{-9}	0	0.1737×10^{-9}
150	0.0257×10^{-9}	0.1483×10^{-9}	0.1740×10^{-9}
225	0.0254×10^{-9}	0.1486×10^{-9}	0.1740×10^{-9}

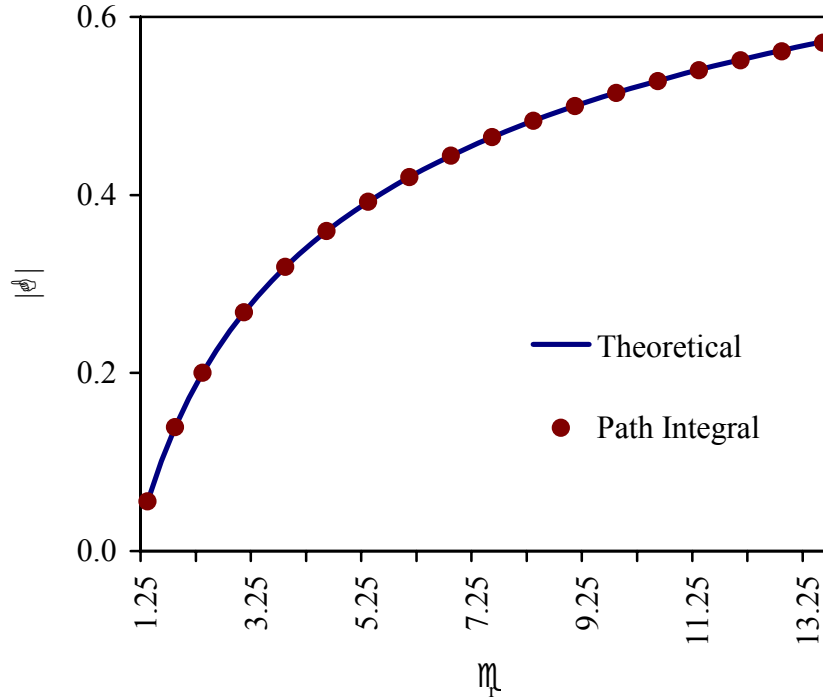


Figure 3. Absolute value of reflection coefficient from dielectric half space as a function of permittivity

Selecting the Time Step

The natural time step produces good results (Figure 2). The question remains for a problem with multiple regions as to which phase velocity to use in determining the time step. Previously the free space phase velocity determined the time step.

Figure 4 shows a set of time steps corresponding to the last pair in Figure 2 when the phase velocity of the dielectric determines the time step. Notice that the scattered field becomes jittery after reflecting from the half space. The specified time step causes the field components to traverse a single spatial step per time step inside the dielectric region. The same time step moves the field more than a single spatial amount in the free space region. The time step ($\tau = \Delta/c$) moves the field a single spatial step per time step in the free space region while moving the field less than a spatial step per time step in the dielectric. Table 5 lists the energy density for the four time steps using the time step ($\tau = \Delta\sqrt{\epsilon_r}/c$). The percent error for time steps 65 and 160 are 2.99% and 2.94%, respectively.

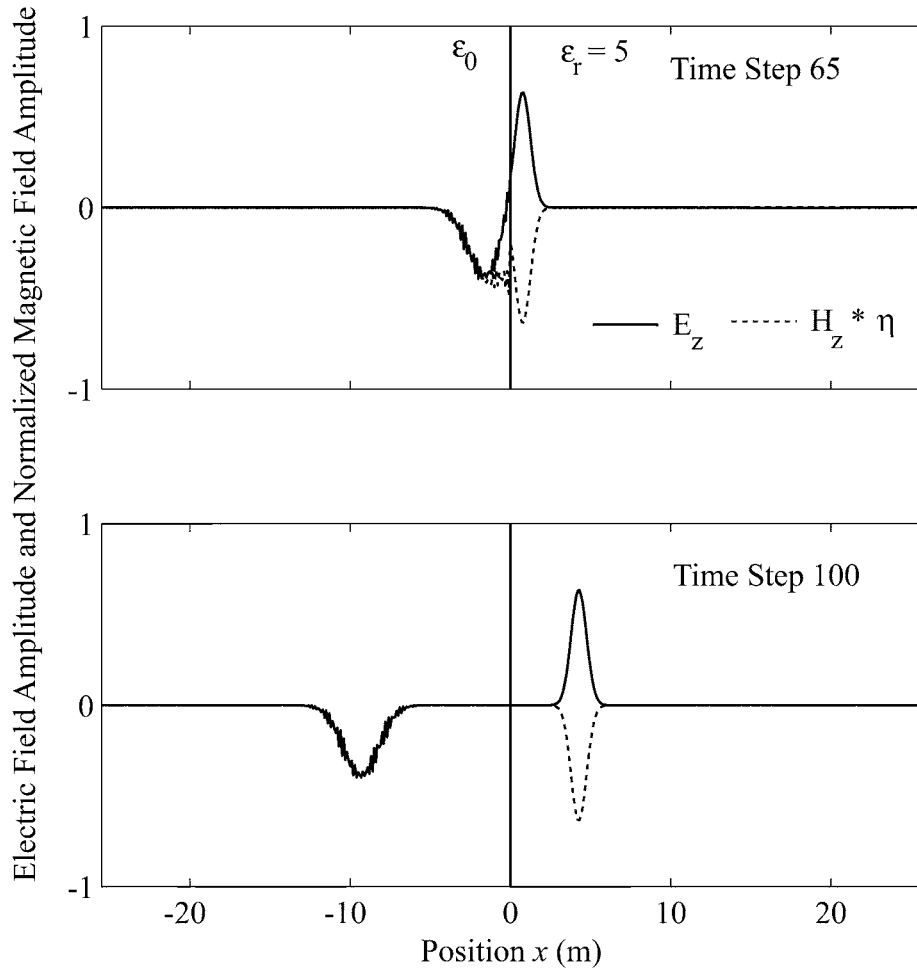


Figure 4. Reflection and transmission from a dielectric half space with natural time step in dielectric

Table 5. Energy density for a dielectric half space with natural time step in dielectric

Time Step	Free Space	Dielectric $\epsilon_r = 5$	Total
0	0.1737×10^{-9}	0	0.1737×10^{-9}
35	0.1737×10^{-9}	0	0.1737×10^{-9}
65	0.0273×10^{-9}	0.1516×10^{-9}	0.1789×10^{-9}
100	0.0261×10^{-9}	0.1527×10^{-9}	0.1788×10^{-9}

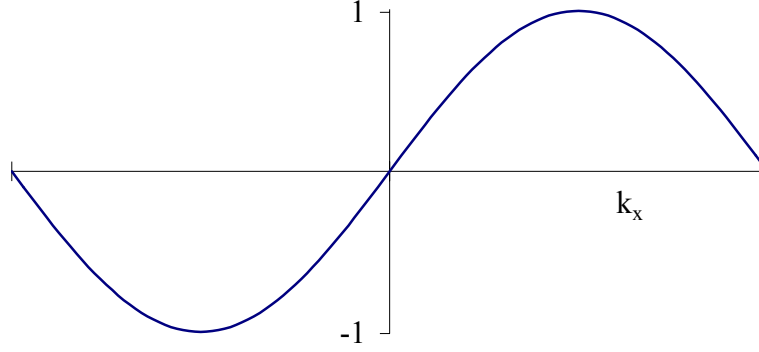


Figure 5. Natural time step with matching medium phase velocity

Carefully examining the state transition matrix elements shows how the time step relates to physical discretization. Choosing the sine term from the state transition matrix since it has a zero at the zero spatial frequency, the range for the natural time step is in Figure 5.

Figure 5 In this case, the time step is $(\tau = \Delta/v_p)$ which reduces the argument of the sinusoid to

$$u = 2\pi k_x v_p \tau = 2\pi k_x v_p (\Delta/v_p) = 2\pi k_x \Delta. \quad (44)$$

After putting equation (28) into (44) and letting n represent the discrete points, u becomes

$$u = 2\pi (n \Delta k_x) \Delta = 2\pi \left(\frac{n}{N \Delta} \right) \Delta = 2\pi \left(\frac{n}{N} \right). \quad (45)$$

Since n takes values between $-N/2$ and $N/2$, u has values between $-\pi$ and π . Therefore, the sinusoids encompass one complete cycle. Using the natural time step of free space inside a dielectric region with a greater permittivity gives an incomplete cycle as seen in

Figure 6.

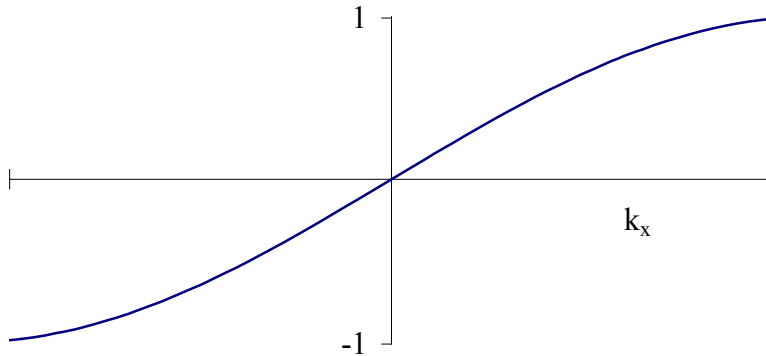


Figure 6. Different phase velocities between time step and media

This mismatch between the phase velocities of the time step and the medium gives

$$u = 2\pi k_x v_p \tau = 2\pi k_x v_p \left(\frac{\Delta}{c} \right) = 2\pi k_x \frac{c}{\sqrt{\epsilon_r}} \frac{\Delta}{c} = 2\pi k_x \frac{\Delta}{\sqrt{\epsilon_r}}. \quad (46)$$

Once again replacing k_x with its discrete equivalent and using (28), the argument becomes

$$u = 2\pi \left(\frac{n}{N\Delta} \right) \frac{\Delta}{\sqrt{\epsilon_r}} = 2\pi \left(\frac{n}{N\sqrt{\epsilon_r}} \right). \quad (47)$$

Figure 2 includes the complete and partial sinusoid ranges discussed above. In the dielectric region because of the partial cycle, the field does not propagate a spatial step per time step.

Figure 4 demonstrates the selection of the natural time step for the dielectric region. The sinusoids complete more than a cycle for the free space region, causing the field to propagate a single spatial step every time step in the dielectric but greater than a spatial step in the free space region.

Considering a homogeneous space, there are three possible choices for the time increment.

First, the natural time step provides the correct slice of time allowing the field to move a single spatial step.

Second a partial time step allowing the field to traverse a portion of the spatial step.

Third a super time step allowing the field to traverse a distance greater than a spatial step.

In a homogeneous space, any one of these time steps is valid. Figure 7 demonstrates three different time steps propagating an identical Gaussian pulse in a homogeneous space. The three time steps are: natural time step ($\tau = \Delta/v_p$), twice the natural time step ($\tau = 2\Delta/v_p$), and half the natural time step ($\tau = \Delta/2v_p$). The first time slice is the initial pulse. The second and third graphs are at time step 130. The last graph is a representation of the difference between the pulses calculated by matching the peaks of each pulse. D1 is the difference between the natural time step and twice the natural time step. D2 is the difference between the natural time step and half the natural time step. In both cases, the difference is at machine precision.

In an inhomogeneous space, the data above promotes two guidelines for selecting the spatial and temporal discretization. Calculate the natural time step using the fastest phase velocity (lowest relative permittivity and permeability). This ensures that at most a single spatial step is covered per time step in any region. The slowest phase velocity region determines the physical discretization based on highest frequency and Nyquist limit.

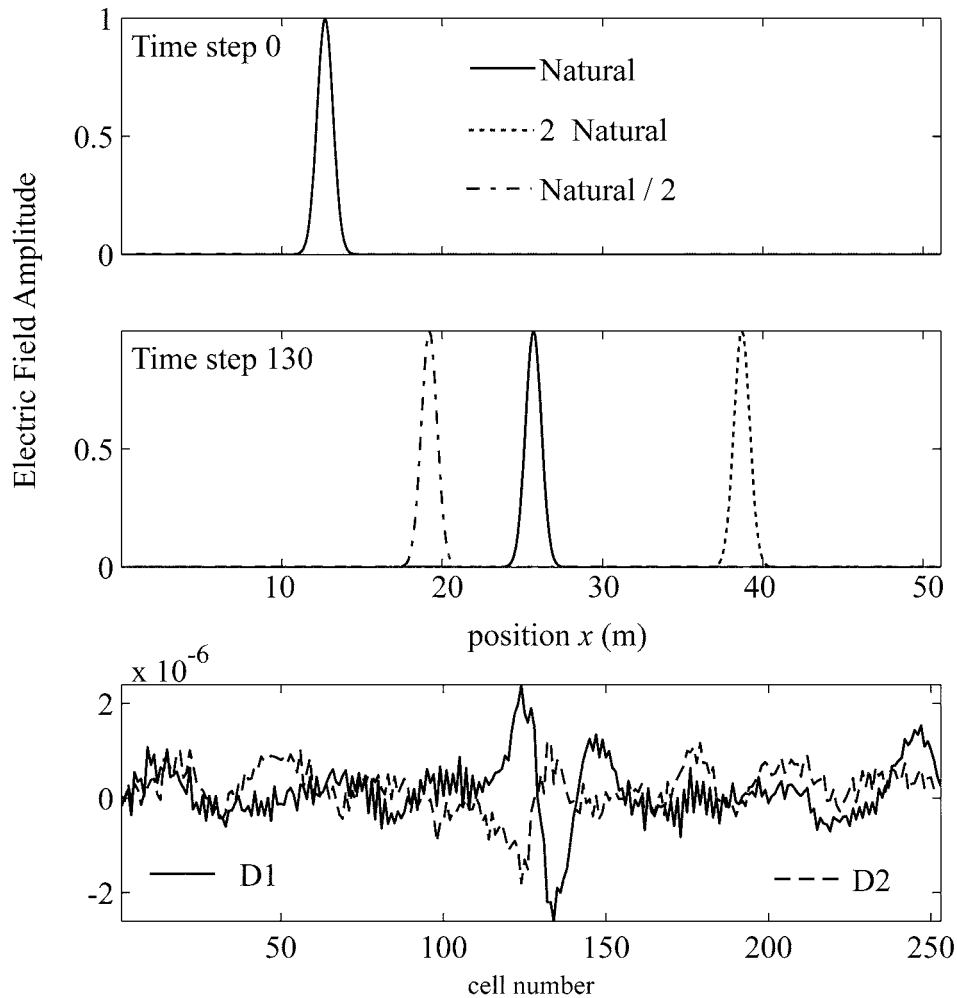


Figure 7. Time step comparison for homogeneous space

Propagation at the Nyquist Limit

The Nyquist limit is a limit numerical techniques strive to achieve. The fewer samples per wavelength a method requires translates into smaller numerical problem sizes and faster run times. The PITD method achieves propagation at the Nyquist limit in homogeneous space, as shown in Figure 8. The sample size is 0.5 meter with a time step of $\Delta/2c$ in a free space homogeneous region. The theoretical curve of a Gaussian ramped sinusoid contains many more points than the two points per wavelength of the PITD simulation. The data shows the results after propagating 1000 time steps or 500 spatial points. Propagation at the Nyquist limit is a very exciting aspect of the PITD method. When considering inhomogeneous space, the limit would apply to the slowest phase velocity material

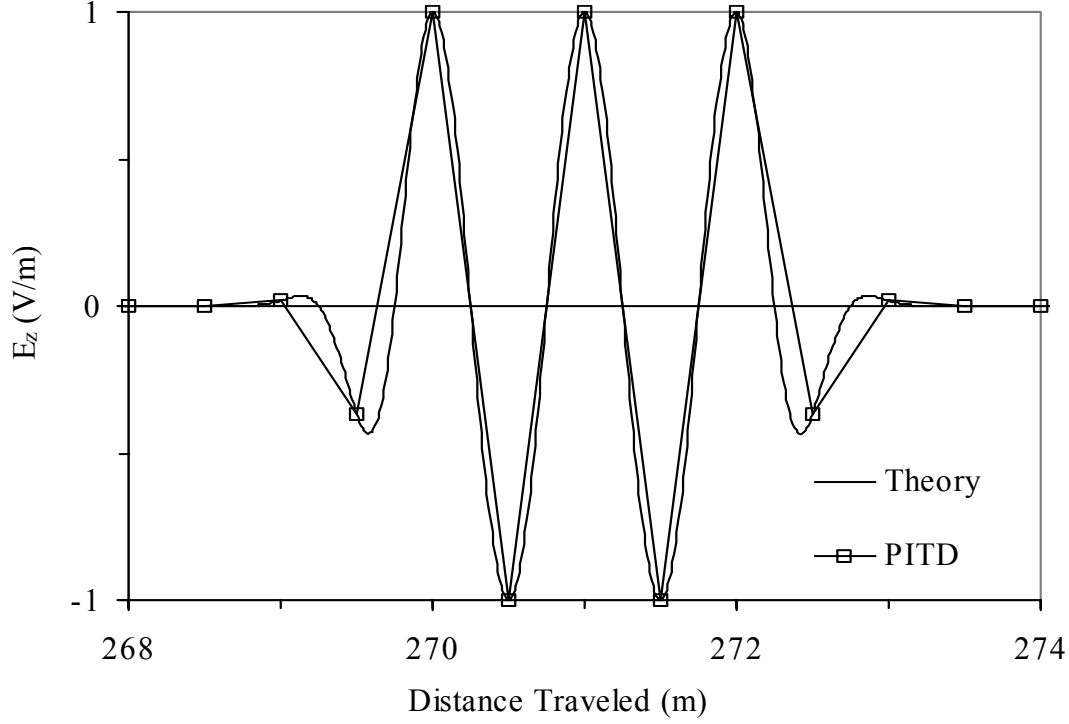


Figure 8. Nyquist limit propagation in one dimension

Explicit Form

Careful examination of (37) shows the inverse Fourier transform of the product of two objects. Instead of multiplying these objects in the spectral domain, equivalently, one may convolve them in the space domain giving

$$\begin{bmatrix} E_z(x,t) \\ H_y(x,t) \end{bmatrix} = \int_{-\infty}^{\infty} \mathcal{F}^{-1} \left\{ \begin{bmatrix} \cos(u) & j\eta \sin(u) \\ (j/\eta) \sin(u) & \cos(u) \end{bmatrix} \right\} \begin{bmatrix} E_z(x-\lambda, t') \\ H_y(x-\lambda, t') \end{bmatrix} d\lambda \quad (48)$$

with $u = 2\pi k_x v_p \tau$. The inverse spatial Fourier transform of the state transition matrix is

$$\frac{1}{2} \begin{bmatrix} \delta(\lambda - v_p \tau) + \delta(\lambda + v_p \tau) & -\eta(\delta(\lambda - v_p \tau) - \delta(\lambda + v_p \tau)) \\ -(\delta(\lambda - v_p \tau) - \delta(\lambda + v_p \tau))/\eta & \delta(\lambda - v_p \tau) + \delta(\lambda + v_p \tau) \end{bmatrix}. \quad (49)$$

Performing the convolution, (48) becomes

$$\begin{bmatrix} E_z(x,t) \\ H_y(x,t) \end{bmatrix} = \frac{1}{2} \begin{bmatrix} \left(E_z(x - v_p \tau, t') + E_z(x + v_p \tau, t') \right) \\ \left(-\eta(H_y(x - v_p \tau, t') - H_y(x + v_p \tau, t')) \right) \\ \left(-(E_z(x - v_p \tau, t') - E_z(x + v_p \tau, t'))/\eta \right) \\ \left(+H_y(x - v_p \tau, t') + H_y(x + v_p \tau, t') \right) \end{bmatrix}. \quad (50)$$

Equation (50) shows that the current electric field is the average of the previous electric field from both sides and the difference of the magnetic field multiplied by the impedance. The locations from which the previous time data is taken match the phase velocity time step product. Notice that the electromagnetic field is not split into left and right traveling wave, but that the total field for each term on the right hand side of (50) gives the current total field. This is easily transferred into the discrete equations by replacing τ with the natural time step Δ/v_p giving

$$\begin{bmatrix} E_z(m\Delta, t) \\ H_y(m\Delta, t) \end{bmatrix} = \frac{1}{2} \begin{bmatrix} \left(E_z((m-1)\Delta, t') + E_z((m+1)\Delta, t') \right) \\ \left(+\eta(H_y((m+1)\Delta, t') - H_y((m-1)\Delta, t')) \right) \\ \left((E_z((m+1)\Delta, t') - E_z((m-1)\Delta, t'))/\eta \right) \\ \left(+H_y((m-1)\Delta, t') + H_y((m+1)\Delta, t') \right) \end{bmatrix}. \quad (51)$$

In (51), the impedance on the right hand side is determined by the location of the left hand field point. The implicit form of the PITD method (performing the Fourier transforms) requires a regular spatial discretization and temporal discretization assuming standard transforming techniques are used. As previously discussed, this regular gridding may result in the field being interpolated between sampling points. For the explicit form (no Fourier transforms), the same time step is kept for all regions. This allows the spatial sampling to change dependent upon the phase velocity. Once again, the actual interface between the two regions is not a sample point. The interface occurs between two of the data points.

Figure 9 shows the same four time steps as the first example.

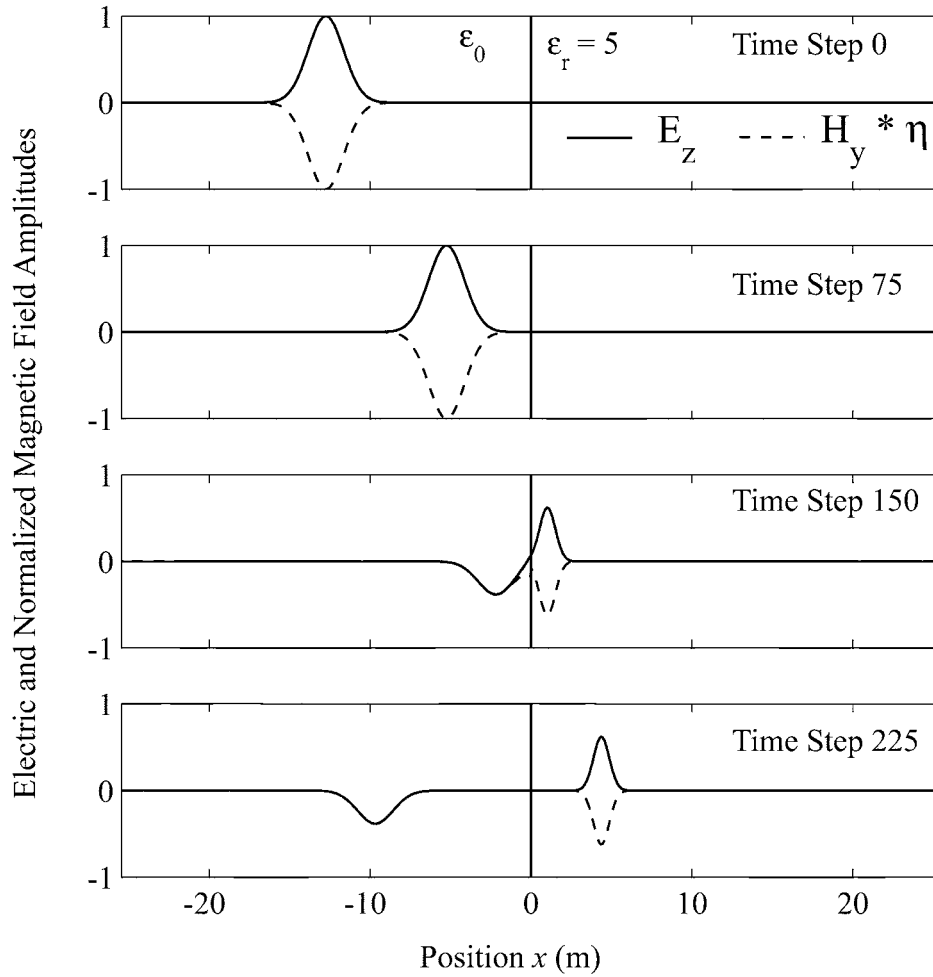


Figure 9. Explicit form showing reflection and transmission for a dielectric half space

The numerical parameters for the explicit form are similar to those in Table 3 with the difference being the spatial discretization in the dielectric region. The spatial sampling in the dielectric region is $\Delta/\sqrt{\epsilon_r}$. The number of samples in the dielectric region was increased from 256 to 570 giving the same physical space. The reflection and transmission coefficients along with percent error are in Table 6. The reflection coefficient is slightly more accurate using the explicit form.

Table 6. Reflection and transmission coefficient for explicit form

Time Step	Reflection Coefficient	Percent Error	Transmission Coefficient	Percent Error
150	-.3822	0.052 %	.6191	0.162 %
225	-.3826	0.157 %	.6191	0.162 %

The energy density for the explicit form matched those of the implicit form in Table 4. The explicit form is a promising area of research for the PITD method.

Lossy Materials

Maxwell's equations in matrix form for a general lossy isotropic region are

$$\frac{\partial}{\partial t} \begin{bmatrix} E_z \\ H_y \end{bmatrix} = \begin{bmatrix} \frac{-\sigma}{\epsilon} & \frac{1}{\epsilon} \frac{\partial}{\partial x} \\ \frac{1}{\mu} \frac{\partial}{\partial x} & \frac{-\rho}{\mu} \end{bmatrix} \begin{bmatrix} E_z \\ H_y \end{bmatrix}. \quad (52)$$

The $\bar{\mathbf{S}}(x, k_x)$ matrix including (13) is

$$\bar{\mathbf{S}}(x, k_x) = \begin{bmatrix} \frac{-\sigma}{\epsilon} & \frac{j2\pi k_x}{\epsilon} \\ \frac{j2\pi k_x}{\mu} & \frac{-\rho}{\mu} \end{bmatrix}. \quad (53)$$

In (53), the material parameters $(\epsilon, \mu, \sigma, \rho)$ are functions of position and $k \equiv k_x$. The eigenvalues and eigenvectors of $\bar{\mathbf{S}}(x, k_x)$ are in Table 7.

Table 7. Eigenvalues and eigenvectors for 1-D lossy problems

	Eigenvalue	Eigenvector
1	$\frac{-1}{2} \left(\frac{\sigma}{\epsilon} + \frac{\rho}{\mu} - \zeta \right)$	$\begin{bmatrix} \frac{j\mu}{4\pi k_x} \left\{ \frac{-\sigma}{\epsilon} + \frac{\rho}{\mu} + \zeta \right\} \\ 1 \end{bmatrix}$
2	$\frac{-1}{2} \left(\frac{\sigma}{\epsilon} + \frac{\rho}{\mu} + \zeta \right)$	$\begin{bmatrix} \frac{j\mu}{4\pi k_x} \left\{ \frac{-\sigma}{\epsilon} + \frac{\rho}{\mu} - \zeta \right\} \\ 1 \end{bmatrix}$
Note: $\zeta = \sqrt{\left(\frac{-\sigma}{\epsilon} + \frac{\rho}{\mu} \right)^2 - (4\pi k_x v_p)^2}$		

Putting the eigenvalues and eigenvectors from Table 7 into (16) generates the state transition matrix

$$\bar{\mathbf{A}} = \begin{bmatrix} a_{11} & a_{12} \\ a_{21} & a_{22} \end{bmatrix} \quad (54)$$

with

$$a_{11} = \left\{ \cosh\left(\frac{1}{2}\zeta\tau\right) + \frac{\frac{-\sigma}{\epsilon} + \frac{\rho}{\mu}}{\zeta} \sinh\left(\frac{1}{2}\zeta\tau\right) \right\} e^{\frac{-1}{2}\left(\frac{\sigma}{\epsilon} + \frac{\rho}{\mu}\right)\tau}, \quad (55)$$

$$a_{12} = \frac{j4\pi k_x}{\varepsilon\zeta} \sinh\left(\frac{1}{2}\zeta\tau\right) e^{\frac{-1}{2}\left(\frac{\sigma+\rho}{\varepsilon+\mu}\right)\tau}, \quad (56)$$

$$a_{21} = \frac{j4\pi k_x}{\mu\zeta} \sinh\left(\frac{1}{2}\zeta\tau\right) e^{\frac{-1}{2}\left(\frac{\sigma+\rho}{\varepsilon+\mu}\right)\tau}, \quad (57)$$

and

$$a_{22} = \left\{ \cosh\left(\frac{1}{2}\zeta\tau\right) + \frac{\frac{\sigma}{\varepsilon} - \frac{\rho}{\mu}}{\zeta} \sinh\left(\frac{1}{2}\zeta\tau\right) \right\} e^{\frac{-1}{2}\left(\frac{\sigma+\rho}{\varepsilon+\mu}\right)\tau}. \quad (58)$$

ζ (defined in Table 7) reduces (55)-(58) to a manageable size. Letting both the conductivity (σ) and resistivity (ρ) go to zero returns the lossless state transition matrix. Selecting the geometry in Figure 1 but replacing the dielectric region with a lossy dielectric specified in Table 8 provides the results in Figure 10. The reflection coefficient is -0.382 which agrees with the theoretical result.

Table 8. General lossy one-dimensional data parameters

N	Δ	τ	ε_r	μ_r	σ	ρ	β
512	0.1 m	Δ/c	5	1	1.328×10^{-4}	3.7699	$7\sqrt{\varepsilon_r}$

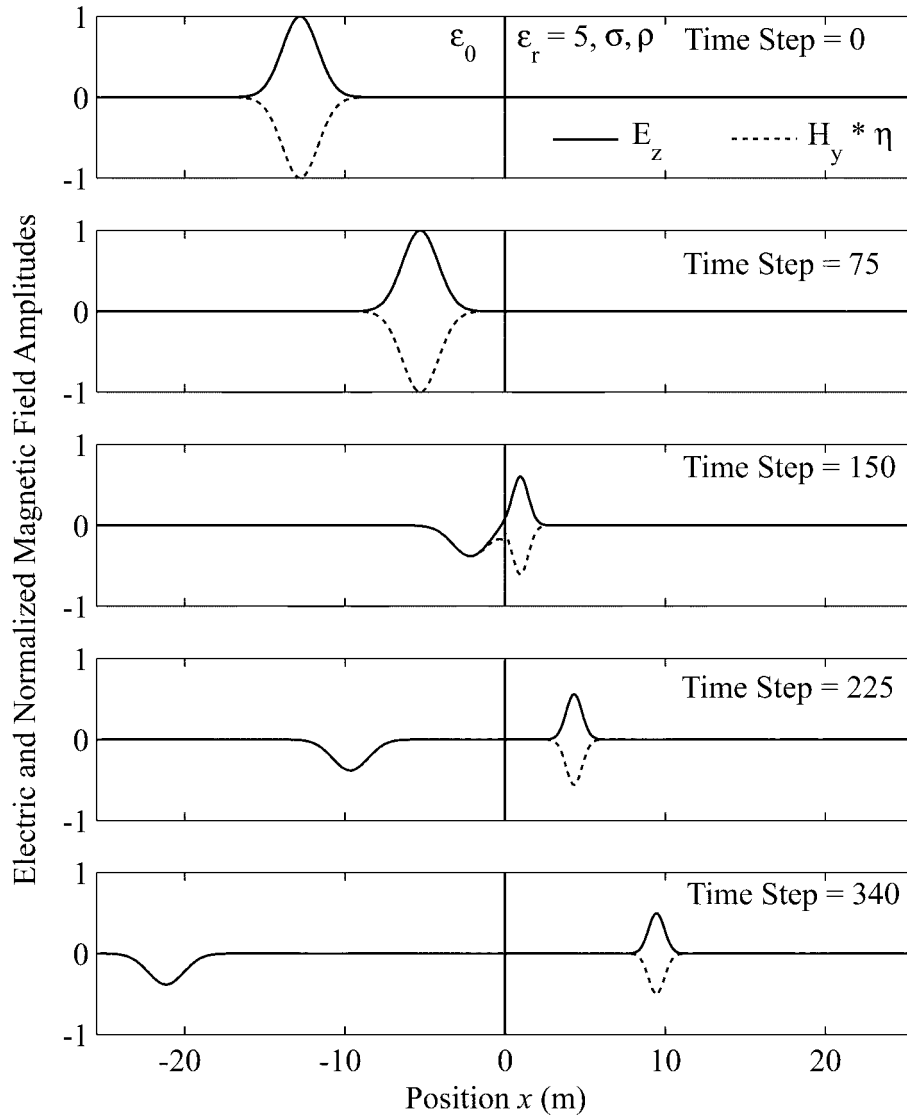


Figure 10. Reflection and transmission from a general lossy half space

Absorbing Boundary Conditions

There are two very effective absorbing boundary conditions (ABC) for the one dimensional PITD method. The first boundary condition is a perfectly matched layer (PML). Berenger [9] extended planar absorbing layers to non-normal incidence, which is an important consideration for higher dimensional spaces. The second boundary condition appears to be unique to the PITD method. It is termed the null boundary (NB) and is the simplest boundary condition to implement. Single dimensional spaces provide a decided advantage when considering ABCs. The field is always normal to the boundary so there is no concern about angle dependence of the reflection coefficient. PML is a series of layers with progressively higher loss but constant impedance. This absorbs the incident wave without reflection. The reflection coefficient (Γ) is calculated from the intrinsic impedances by

$$\Gamma = \frac{\eta_2 - \eta_1}{\eta_2 + \eta_1} \quad (59)$$

where the subscript indicates the region and the field is incident from region 1 into region 2. Obviously, if $\eta_2 = \eta_1$ there is no reflection. In the frequency domain, the intrinsic impedance is a complex value that is frequency and loss (σ, ρ) dependent. For the time-domain, it is essential that the reflection coefficient be constant for all frequencies and zero. Therefore, a relationship between ε, μ, σ , and ρ is needed. Starting with

$$\zeta = \sqrt{\left(\frac{-\sigma}{\varepsilon} + \frac{\rho}{\mu}\right)^2 - (4\pi k_x v_p)^2} \quad (60)$$

and letting

$$\frac{\sigma}{\varepsilon} = \frac{\rho}{\mu} \quad (61)$$

then

$$\begin{aligned} \zeta &= \sqrt{(0)^2 - (4\pi k_x v_p)^2} \\ \zeta &= j4\pi k_x v_p \end{aligned} \quad (62)$$

resulting in

$$\bar{\mathbf{A}} = \begin{bmatrix} \cosh(j2\pi k_x v_p \tau) & \eta \sinh(j2\pi k_x v_p \tau) \\ \sinh(j2\pi k_x v_p \tau)/\eta & \cosh(j2\pi k_x v_p \tau) \end{bmatrix} e^{\frac{-\sigma}{\varepsilon} \tau}. \quad (63)$$

The hyperbolic trigonometric functions of complex argument reduces to normal trigonometric functions of real argument resulting in

$$\bar{\mathbf{A}} = \begin{bmatrix} \cos(2\pi k_x v_p \tau) & j\eta \sin(2\pi k_x v_p \tau) \\ j \sin(2\pi k_x v_p \tau)/\eta & \cos(2\pi k_x v_p \tau) \end{bmatrix} e^{\frac{-\sigma}{\varepsilon} \tau}. \quad (64)$$

Notice equation (64) is the lossless state transition matrix with a multiplication by a loss term. Selecting equation (61) ensures that the impedance is constant in each layer for all frequencies and the loss is a simple exponential multiplier. Following the work of Berenger [9], a nine cell ABC with each layers σ_i a parabolic function of depth defined by

$$\sigma_i = \frac{\sigma_m}{\delta^2} \left((i\Delta)^2 + (\Delta)^2 / 12 \right) \quad (65)$$

where $\delta = 9\Delta$ is the width of the absorbing zone (nine cells) and

$$\sigma_m = \frac{3\varepsilon v_p |\ln R|}{2\delta} \quad (66)$$

with $R = 10^{-5}$. Though PML performance is not demonstrated here, previous works have demonstrated reflectionless performance on the order of machine error.

The null boundary (NB) is one of those accidents of science. It was discovered while examining perfect electric conductors (PEC) in the PITD method. Since the electric and magnetic fields are zero inside a PEC, the field components for sample points inside the conductor are zeroed. When the program ran, the field did not reflect from this “PEC” but instead were absorbed by it. The reason becomes apparent by looking closely at the explicit form (51). Concentrating on the electric field component

$$E_z(m_\Delta, t) = \frac{1}{2} \left(E_z((m-1)_\Delta, t') + E_z((m+1)_\Delta, t') + \eta(H_y((m-1)_\Delta, t') - H_y((m+1)_\Delta, t')) \right), \quad (67)$$

the current time electric field at location m is the average of the electric field on either side plus the half of the difference of the magnetic field multiplied by the impedance at m . Now assume that the “PEC” is to the right of m , the field is always zero and (67) reduces to

$$E_z(m_\Delta, t) = \frac{1}{2} \left(E_z((m-1)_\Delta, t') + \eta H_y((m-1)_\Delta, t') \right). \quad (68)$$

A field $E_z(m, t)$ at the boundary is therefore only computed from the field to the left of the boundary. No reflection occurs, because the field at the boundary can only travel into the boundary. Equation (68) is also the equation obtained for the leading point of a plane wave traveling in space. Having discovered this ABC by accident, a question remains concerning its effectiveness. The boundary is actually a single cell on either end of the space.

Table 9. One-dimensional ABC numerical parameters

N	Δ	τ	ϵ_r	μ_r	β	PML	NB
512	0.1 m	Δ/c	1	1	$7\sqrt{\epsilon_r}$	9 cell ABC	1 cell ABC

The null boundary condition has consistently demonstrated equivalent performance to the PML absorbing boundary within machine precision.

Conclusion

The PITD method is a numerical technique still in its infancy. It has several intriguing properties as well as straightforward physical discretization. No sample point lies on a physical boundary between inhomogeneous spaces. This avoids complicating the method development or the ‘ordering problem’ of needing to apply the differential operators in \bar{S} to both the material parameters and the field.

The PITD method is stable and a unitary operation. In a homogeneous space, the only numerical error derives from the finite precision math of the computer and the Fourier transform. This indicates that the PITD method is accurate to the machine precision. The small error found in reflection and transmission through a half space are linked to the inexact location of the interface. The PITD method requires sampling at the Nyquist limit, which is two samples per wavelength at

the highest frequency of interest. This is a very significant factor since most numerical techniques require sampling much finer than the Nyquist limit. The explicit form does not require any numerical Fourier transforms. The PITD method does not suffer from numerical dispersion.

The time step choice is important for inhomogeneous spaces but open for homogeneous space. The natural time step for a homogeneous space moves the field one spatial step every time step. In an inhomogeneous space, the problem time step should match the natural time step for the fastest phase velocity region of the problem. This choice ensures that the field will not travel more than a spatial step per time step in any regions. The spatial discretization is determined by the Nyquist limit for the highest frequency of interest in the slowest phase velocity region. The range of the sinusoids in the lossless state transition matrix has a simple relationship determining the field's spatial movement. A complete cycle moves the field a spatial step per time step, less or more than a cycle moves the fields less or more than one spatial step.

Two ABCs show excellent effectiveness in terminating the numerical space. The PML implemented with several layers of lossy material. Fortunately, the loss term is a separate exponential that does not increase the computational cost significantly. The number of layers and the loss profile are both active research areas for other methods as well as this one. The null boundary requires a single cell for application and is computationally effortless.

Recently, Nevels and Jeong [10] reported an explicit form for a general one-dimensional lossy material. This has wide application in transmission line studies. At its current state of development, the PID method is well suited for one-dimensional problems. It is especially straightforward in illustrations for pedagogical purposes.

REFERENCES

- [1] R. Nevels, J. Miller, and R. Miller, "A path integral time-domain method for electromagnetic scattering," *IEEE Trans. Antennas Propagat.*, vol. AP-48, no. 4, pp. 565-573, April 2000.
- [2] G. Barton, *Elements of Green's Functions and Propagation: Potentials, Diffusion, and Waves*, New York: Oxford University Press, 1995.
- [3] P. DeRusso, R. Roy, and C. Close, *State Variables for Engineers*, New York: John Wiley & Sons, 1965.
- [4] D. M. Wiberg, *Schaum's Outline of Theory and Problems of State Space and Linear Systems*, New York: McGraw-Hill, 1971.
- [5] R. Ziemer, W. Tranter, and D. Fannin, *Signals and Systems: Continuous and Discrete*, New York: Macmillan Publishing Co., 1983.
- [6] W. Press, S. Teukolsky, W. Vetterling, and B. Flannery, *Numerical Recipes in C: The Art of Scientific Computing*, Cambridge: Cambridge University Press, 1992.
- [7] R. Nevels, J. Miller, and R. Miller, "Rotation in Electromagnetic Field Equations: A Discussion, Interpretation and Application," *Digest of the 1998 IEEE AP-S/URSI International Symposium*, Atlanta, Georgia, June 1998, pp. 875-878.
- [8] J. D. Kraus and K. R. Carver, *Electromagnetics*, Tokyo: McGraw-Hill Kogajusha, 1981.
- [9] J.-P. Berenger, A perfectly matched layer for the absorption of electromagnetic waves, *J. Computational Physics*, vol. 114, no. 2, pp. 185-200, Oct. 1994.
- [10] R. D. Nevels and J. Jeong, "The electromagnetic field in a 1-D lossy medium based on a maxwell equation propagator," *Digest of the 2004 IEEE AP-S/URSI International Symposium*, Monterey, California, June 2004, pp. 2055-2058.

COPLANAR WAVEGUIDE FED BOW-TIE SLOT ANTENNAS FOR WIDEBAND OPERATIONS

Abdelnasser A. Eldek, Atef Z. Elsherbeni, and Charles E. Smith

Center of Applied Electromagnetic Systems Research (CAESR)

Department of Electrical Engineering

The University of Mississippi

University, MS 38677, USA

ABSTRACT: *A bow-tie slot antenna with tapered connection to a 50Ω coplanar waveguide (CPW) feed line is introduced and its dimensional parameters have been studied for wideband operations in the X-band. A set of two element bow-tie slot antennas fed by one CPW is also introduced for wider bandwidth and improved gain. The configuration of one CPW feeding two elements of this antenna is simulated and it achieved 50% impedance bandwidth. Measurements of the return loss confirmed the simulation results for the single and the two element slot bow-tie designs.*

Keywords: Bow tie, wideband, coplanar waveguide, slot antennas, radar applications.

1. Introduction

Printed slot antennas fed by a coplanar waveguide (CPW) have many advantages over microstrip antennas. Besides small size, light weight, low cost, good performance, ease of fabrication and installation, and low profile, they exhibit wider bandwidth, lower dispersion and lower radiation loss than microstrip antennas besides the ease of being shunted with active and passive elements required for matching and gain improvement [1].

Bow-tie and bow-tie slot antennas are good candidates for wideband applications. A number of designs are introduced in [1-6] to demonstrate wide bandwidth capabilities that range from 17% to 40%. In this paper, a bow-tie slot antenna geometry with tapered feed line is studied and designed for wideband operation for radar applications. The related simulation and analysis are performed using the commercial computer software package, Momentum of Agilent Technologies, Advanced Design System (ADS), which is based on the method of moment (MoM) technique for layered media. The ADS simulator, Momentum, solves mixed potential integral equations (MPIE) using full wave Green's functions [7].

2. Element Geometry and Analysis

The geometry of the bow-tie slot antenna and its parameters are shown in Fig. 1. The tapering from the CPW to the bow-tie slot is to achieve better matching with a 50Ω feed line. The antenna is studied for 1.57 mm substrate with $\epsilon_r = 2.2$ and the CPW feed line and slot widths are 3 and 0.25 mm, respectively, and its length is 18.5mm. The parameters of the antenna are the outer slot size W_1 and L_1 , and L_2 , L_3 and W_2 that control the bow-tie flair angle and the tapering of the feed line. For the parametric study, W_1 , W_2 , L_1 , L_2 and L_3 are chosen to be 22.9, 1.25, 7.35, 0.95 and 2.25 mm, respectively, and only one parameter is changed at a time during the analysis. Figure 2 shows the effect of changing W_1 , where it is clear that increasing W_1 shifts the operating band to a lower frequency range. As shown in Figures 3, 4 and 5, the parameters W_2 , L_1 and L_2 control the level of the return loss at the main resonance frequency.

Figure 6 shows the effect of changing $L3$. As $L3$ decreases, the resonance frequency shifts higher and the bandwidth increases. This behavior is due to the fact that when $L3$ decreases the bow-tie flair angle increases.

A prototype of the bow-tie slot antenna is fabricated and the return loss is measured using the HP 8510C vector network analyzer (VNA). The fabricated antenna has a finite ground plane truncated at 1 cm away from the bow-tie slot edge. The antenna with the connector is simulated using ADS Momentum and Fig. 7 shows a good agreement between the measured and simulated return loss of this fabricated antenna. According to the measured results, the finite ground plane bow-tie slot antenna has two operating frequency bands centered at 8.3 and 11.7 GHz with bandwidths 18% and 17.4%, respectively.

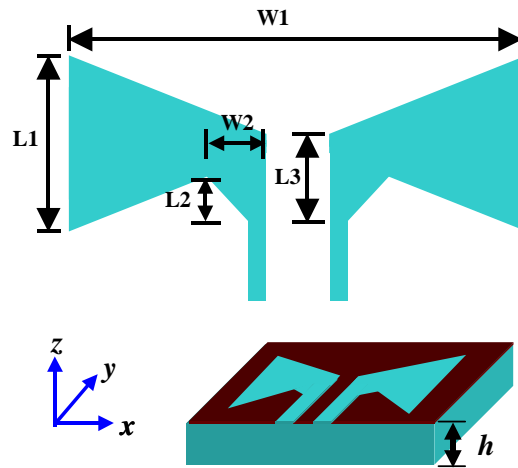


Fig. 1. Antenna geometry and parameters.

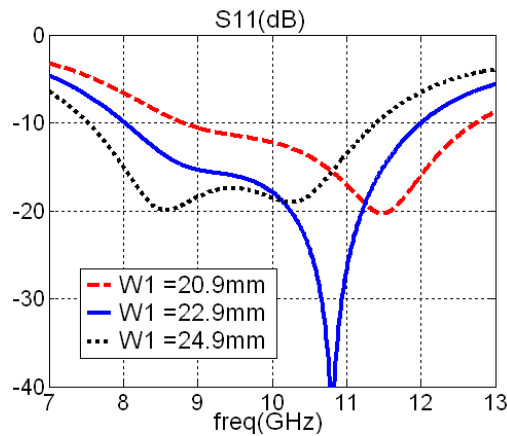


Fig. 2. The effect of changing $W1$.

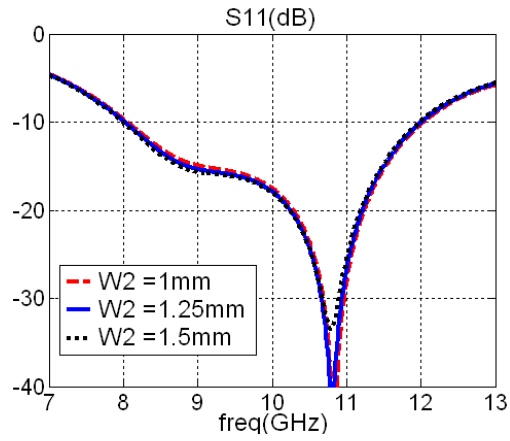


Fig. 3. The effect of changing W_2 .

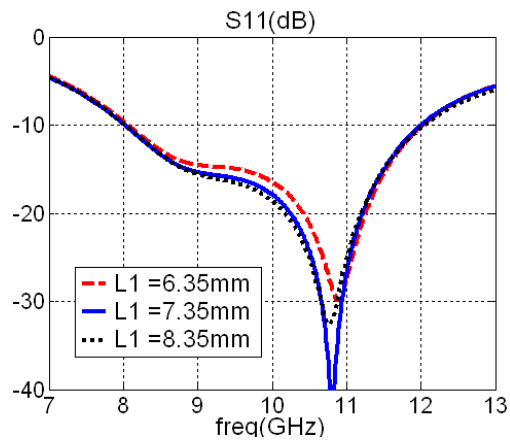


Fig. 4. The effect of changing L_1 .

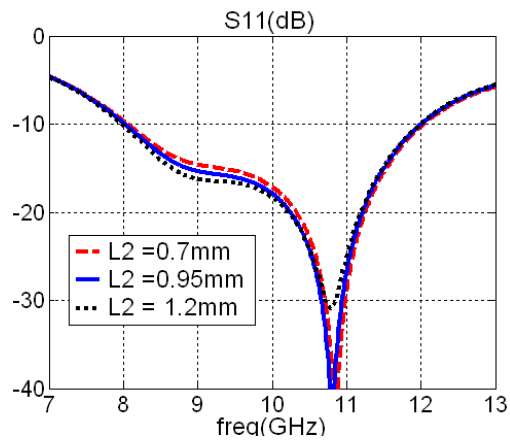


Fig. 5. The effect of changing L_2 .

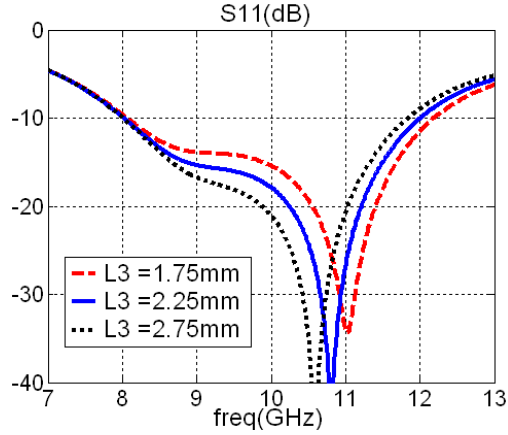


Fig. 6. The effect of changing L3.

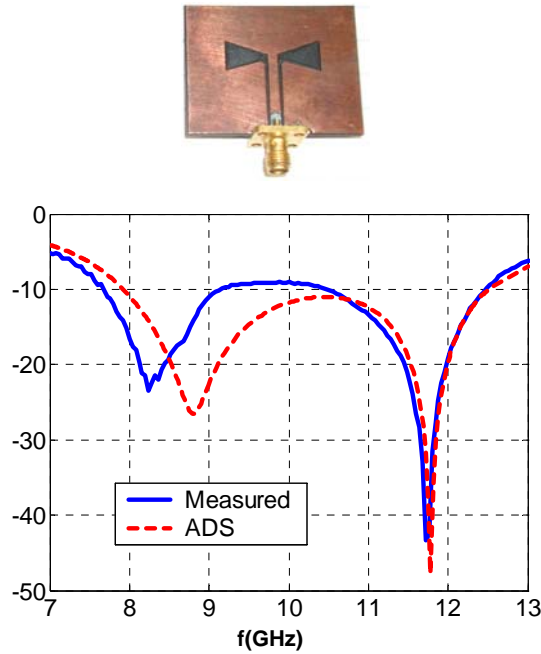


Fig. 7. Comparison between the measurement results and ADS results for the modified bow-tie slot antenna.

3. Two Elements with One CPW Feed

The study of the CPW-to-CPW transition between two different lines and the effect of deformed feed line in [8] is used here to connect the two bow-tie slot antennas with one CPW. Two Elements of the bow-tie slot antenna with W_1 , W_2 , L_1 , L_2 and L_3 chosen to be 22.9, 1.25, 7.35, 0.95 and 2.25 mm, respectively, over a substrate of 1.57 mm thickness and $\epsilon_r = 2.2$, is simulated. The return loss for this combination is shown in Fig. 8. The design provides wider bandwidth over the single element as the antenna operates from 8.7 to 14.5 GHz with approximately 50% bandwidth. The feeding mechanism is similar to that in Fig. 9; however, the center-to-center distance between the two antennas is 26.72 mm and the single element feed line

is kept at 18.5 mm. Another combination of two bow-tie slot antennas is designed for a substrate of $\epsilon_r = 3.38$ and 60 mil height, connected to one CPW feed line as shown in Fig. 9. This design is fabricated and measured, and the picture of the antenna and the comparison between the measured and computed return loss are shown in Fig. 10. According to the measurements, this configuration operates from 7.1 to 10.7 GHz with 40% bandwidth, with a good agreement between simulation and measurements results.

The radiation pattern of the last design is calculated using ADS Momentum at 10 GHz. Figures 11 and 12 show the radiation patterns in the x-z and y-z, respectively, for this antenna. In y-z plane there is no E_ϕ because of the symmetry of the antenna. The cross polarization level is less than -40 dB in the z-direction. The calculated gain and directivity of this antenna are 7.12 dB and 8.268 dB, respectively, and the resulting efficiency is 77%.

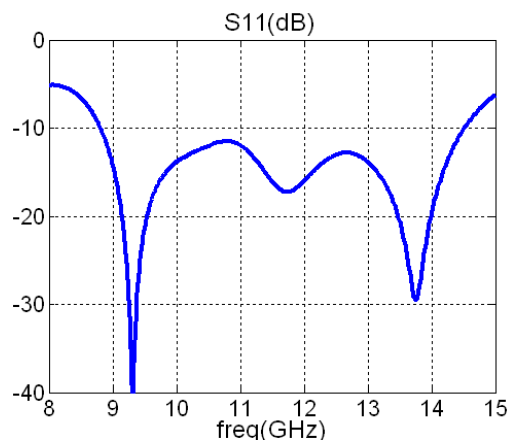


Fig. 8. Return loss of two bow-tie slot antennas connected to one CPW on a substrate with 1.57 mm height and $\epsilon_r = 2.2$.

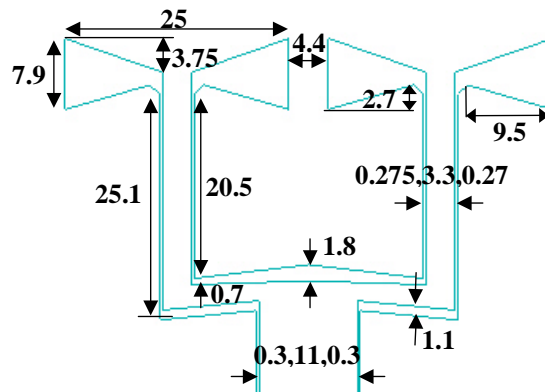


Fig. 9. Geometry and dimensions in mm of the two bow-tie slot antennas fed by one CPW.

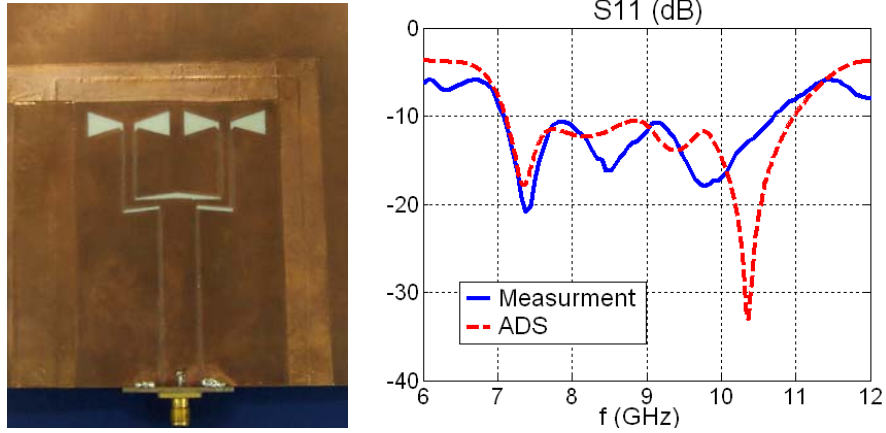


Fig. 10. Comparison between the measured and ADS return loss for the two bow-tie slot antennas fed by one CPW shown in Fig. 9.

4. Conclusion

A one-element bow-tie slot antenna fed by a 50Ω coplanar waveguide is designed for the X-band operation. The measurements of this antenna show two operating bands centered at 8.3 and 11.7 GHz with bandwidths 18% and 17.4%, respectively. An array combination of two of these antennas fed by one CPW achieved 50% bandwidth from 8.7 to 14.5 GHz. A similar antenna is designed and fabricated with a different substrate board that operates from 7.2 to 10.7 GHz with 40% bandwidth.

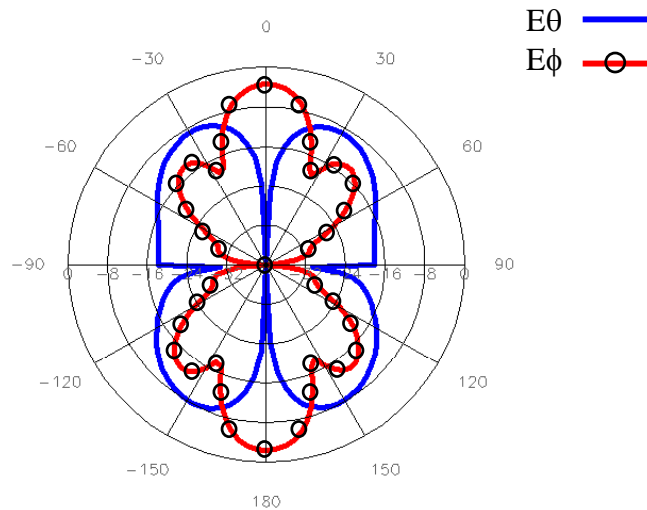


Fig. 11. Far field pattern at in the x-z plane at 10 GHz.

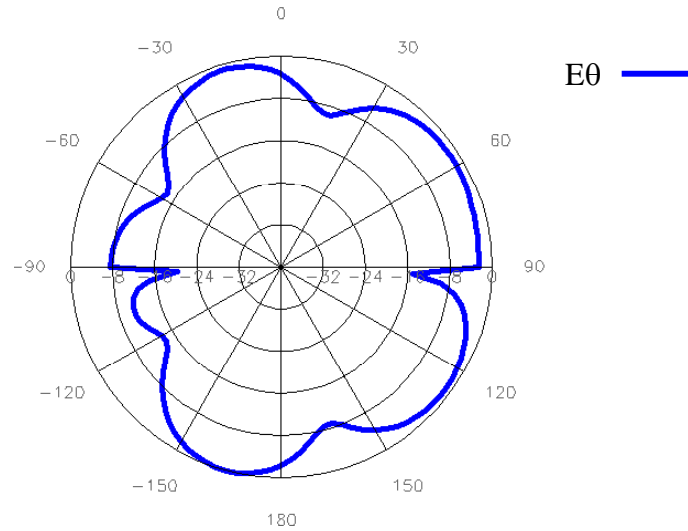


Fig. 12. Far field pattern at in the y-z plane at 10 GHz.

REFERENCES

- [1] Rainee N. Simons, *Coplanar Waveguide Circuits, Components, and Systems*. New York. NY: John Wiley & Sons, Inc., pp. 1-6, pp. 422-424, 2001.
- [2] Yu-De Lin and Syh-Nan Tsai, "Coplanar waveguide-fed uniplanar bow-tie antenna," *IEEE Trans.*, vol. AP-45, no. 2, pp. 305-306, Feb. 2000.
- [3] A. A. Eldek, A. Z. Elsherbeni, C. E. Smith and K-F Lee, "Wideband slot antennas for radar applications," *Proc. IEEE Radar Conf.*, Huntsville, AL, May 2003, pp. 79-84.
- [4] E. A. Soliman, S. Berbels, P. Delmotte, G. A. E. Vandebosch, and E. Beyne, "Bow-tie slot antenna fed by CPW," *Electron Lett.*, vol. 35, pp. 514-515, 1999.
- [5] Jen-Fen Huang, Chih-Wen Kuo, "CPW-fed bow-tie slot antenna," *Microwave Opt. Technol. Lett.*, vol. 19, no. 5, pp. 358-360, Dec. 1998.
- [6] M. Miao, B. L. Ooi, P. S. Kooi, "Broadband CPW-fed wide slot antenna," *Microwave Opt. Technol. Lett.*, vol. 25, no. 3, pp. 206-211, May. 2000.
- [7] Agilent Technologies, Advance Design Systems 1.5 Momentum, Appendix A, December 2000.
- [8] A. A. Eldek, A. Z. Elsherbeni and C. E. Smith, "Analysis of the transition between two coplanar waveguide transmission lines," *ACES newsletter*, vol. 18, no. 2, pp. 44-47, July 2003.

2005 IEEE/ACES International Conference

on Wireless Communications and Applied Computational Electromagnetics

April 3-7, 2005, Hilton Hawaiian Village, Honolulu, Hawaii

Sponsors

IEEE Antennas and Propagation Society (<http://www.ieeeaps.org>),
Applied Computational Electromagnetics Society (<http://aces.ee.olemiss.edu>)
Technically co-sponsored by IEICE Electronics Society, Japan (<http://www.ieice.org/eng/index.html>), and
IEEE Microwave Theory and Techniques Society (<http://www.mtt.org>)



Suggested Technical Topics

Wireless Communications Topics

Phased array antennas
Smart antennas and arrays
UWB systems
MIMO systems
Channel modeling
Wireless testbed
Mobile and PCS antennas
Active antennas
Wideband and multi-frequency antennas
Advanced RF & microwave circuits design
Millimeter wave and terahertz technologies
DOA estimation techniques
Adhoc and adaptive networks

ACES Topics

Low frequency electromagnetic applications
Hybrid techniques
Inverse scattering techniques
Finite element methods
Fast and efficient CEM methods
Wavelet and TLM modeling
Neural network techniques for CEM
Optimization techniques for CEM
Asymptotic and high frequency techniques
Integral Equation Methods
Differential Equation Methods
NEC modeling and analysis
Signal processing antennas

Joint Topics

Time domain methods
Metamaterials
EMC/EMI
MEMS and MMIC
Wave propagation
Radar applications
Computational bio-electromagnetics
Remote sensing applications

Submission Guideline

Authors of original work in the technical areas of interest are encouraged to submit (4) page summary of their work through the electronic submission system available at <http://hcac.hawaii.edu/conferences/ieeeeaces2005/>. Authors should select a technical area of interest for each uploaded paper. Deadline for submission is December 15, 2004.

Steering Committee

General Chair	Magdy F. Iskander (iskander@spectra.eng.hawaii.edu , 808-956-3434)
ACES Co-Chair	Atef Z. Elsherbeni (atef@olemiss.edu , 662-915-5382)
IEEE-APS Co-Chair	Michael A. Jensen (jensen@ee.byu.edu , 801-422-5736)
IEICE, TG-EMT Co-Chair	Makoto Ando (mando@antenna.ee.titech.ac.jp , +81-3-5734-2563)
ACES Liaison	Tapan Sarkar (tsarkar@syr.edu , 315-443-3775)
MTT-S Liaison	Barry S. Perlman (barry.perlman@us.army.mil , 732-427-4883)

For More Information

<http://hcac.hawaii.edu/conferences/ieeeeaces2005/>

ADVERTISING RATES		
	FEE	PRINTED SIZE
Full page	\$200	7.5" × 10.0"
1/2 page	\$100	7.5" × 4.7" or 3.5" × 10.0"
1/4 page	\$50	3.5" × 4.7"
<p>All ads must be camera ready copy.</p> <p>Ad deadlines are same as Newsletter copy deadlines.</p> <p>Place ads with Ray Perez, Newsletter Editor, Martin Marietta Astronautics, MS 58700, PO Box 179, Denver, CO 80201, USA. The editor reserves the right to reject ads.</p>		

DEADLINE FOR THE SUBMISSION OF ARTICLES	
Issue	Copy Deadline
March	February 1
July	June 1
November	October 1

For the **ACES NEWSLETTER**, send copy to Bruce Archambeault in the following formats:

1. A PDF copy.
2. A MS Word (ver. 97 or higher) copy. If any software other than WORD has been used, contact the Managing Editor, Richard W. Adler **before** submitting a diskette, CD-R or electronic file.

Last Word

There are in fact two things, science and opinion; the former begets knowledge, the latter ignorance.

Hippocrates (460 BC - 377 BC)